

Felix Krall

**Analysis and Implementation of Algorithms
for Calculation of Iron Losses for Fractional
Horsepower Electric Motors**

Master's Thesis

Submitted in Partial Fulfillment of the Requirements for the Degree of

**Diplom Ingenieur
(Dipl.-Ing.)**

in

Electrical Engineering

at

Graz University of Technology

In Cooperation with:

Mechatronic Systems GmbH, Wies, Austria

and

Christian Doppler Laboratory for Brushless Drives
for Pump and Fan Applications, Graz, Austria

Univ.-Prof. Dr.-Ing. Annette Mütze

Electric Drives and Machines Institute

Graz University of Technology

2017



Felix Krall, BSc

Analysis and Implementation of Algorithms for Calculation of Iron Losses for Fractional Horsepower Electric Motors

MASTER'S THESIS

to achieve the university degree of

Diplom-Ingenieur

Master's degree programme: Electrical Engineering

submitted to

Graz University of Technology

Supervisor

Univ.-Prof. Dr.-Ing. Annette Mütze

Electric Drives and Machines Institute

AFFIDAVIT

I declare that I have authored this thesis independently, that I have not used other than the declared sources/resources, and that I have explicitly indicated all material which has been quoted either literally or by content from the sources used. The text document uploaded to TUGRAZonline is identical to the present master's thesis.

Date

Signature

Contents

Abstract	V
Zusammenfassung (in German)	VII
1 Short overview of iron loss models	1
1.1 Introduction	1
1.2 Steinmetz based models	1
1.2.1 Modified Steinmetz Equation - MSE	3
1.2.2 Generalized Steinmetz Equation - GSE	4
1.2.3 improved Generalized Steinmetz Equation - iGSE	5
1.2.4 Natural Steinmetz Extension - NSE	5
1.2.5 improved improved Generalized Steinmetz Equation - i^2 GSE .	6
1.2.6 Other Steinmetz based methods	7
1.3 Loss surface model	8
1.4 Loss separation approach	9
1.5 Physically based methods	10
1.5.1 Preisach model	11
1.5.2 Jiles Atherton model	13
1.6 Conclusion	14
2 Iron loss calculation with the iGSE	17
2.1 Introduction	17
2.2 Nested loop algorithm	17
2.3 Equations	20
2.4 Verification based on simple signals	21
2.4.1 Testsignal 1 - Combined triangular signal	21
2.4.2 Testsignal 2 - Sinusoidal Signal	25
2.4.3 Testsignal 3 - Approximation of a yoke flux density	28
2.5 Brute force parameter fit	30

2.6	Conclusion	35
3	Loss surface model	37
3.1	Introduction	37
3.2	Principle idea	37
3.3	Measurement waveform	39
3.4	Measurement setup	43
3.4.1	Measurement equipment	44
3.4.2	Measurement process	44
3.4.3	Internal controller	46
3.5	Calculations	51
3.6	Evaluation of the measurement results	52
3.6.1	Measurement accuracy	53
3.7	Interpolation	55
3.7.1	Inverse distance weighted interpolation - IDWI	56
3.7.2	Thin plate spline interpolation - TPSI	57
3.8	Considerations regarding the Epstein frame	60
3.8.1	Effective magnetic path length	62
3.9	Conclusion	63
4	Comparison of the iGSE and the loss surface approach	65
4.1	Introduction	65
4.2	Waveforms	65
4.3	Results	68
4.3.1	Results of the iGSE	68
4.3.2	Results of the loss surface approach	69
4.4	Conclusion	73
5	Outlook and further steps	75
5.1	Iterative learning control - ILC	75
5.1.1	Desired distribution of the flux density	77
5.2	Ring shaped specimen	80
5.2.1	FEM simulations for the ring shaped specimen	81
5.3	Conclusion	82
	Bibliography	83

List of figures	87
List of tables	89

Abstract

The iron losses in an electrical machine represent a large portion of the total losses having thereby essential influence on the efficiency. Without any measurements the iron losses cannot be described as simple analytically as the copper losses. If no measurement data are provided, approximation-based methods have to be used.

The aim of this thesis is to find, implement and verify suitable iron loss calculation methods, for fractional horse power drives. At the beginning, a thorough literature research gives an overview on different iron loss calculation methods. Reaching from simple Steinmetz-based methods to measurement-based approaches to physico-mathematical methods. As the next step, two selected iron loss calculation procedures are explained in detail. The first one, the improved generalized Steinmetz equation (iGSE), is a Steinmetz-based approach and requires Steinmetz parameters only, which can easily be determined from the iron loss curves of the data sheet when needed. The second method, the loss surface approach, determines a loss surface in the $B\text{-}\frac{dB}{dt}$ room from measurements, which represents the material behavior. Although the loss surface approach is a bit more complex than the iGSE it can also be used for materials where no data sheet is available or if the characteristics of the material are changed due to the cutting process.

Subsequently, the two implemented iron loss calculation methods are tested for different flux density distributions and the results are compared with each other. Finally, it is discussed how to improve the methods accuracy and applicability.

Zusammenfassung

Die Eisenverluste einer elektrischen Maschine stellen einen großen Anteil der gesamten Verluste dar und beeinflussen somit maßgeblich den Wirkungsgrad. Im Gegensatz zu den Kupferverlusten, lassen sich die Eisenverluste nicht so einfach analytisch bestimmen und es muss daher auf Näherungsverfahren oder messtechnisch gestützte Methoden zurückgegriffen werden.

Diese Arbeit beschäftigt sich damit, für Kleinmotoren geeignet erscheinende Bestimmungsmethoden zu finden, zu implementieren und zu testen. Zu Beginn steht eine Literaturrecherche in der der Bogen von einfachen Steinmetz basierten Ansätzen, über messtechnische bis hin zu aufwändigen physikalisch mathematischen Modellen gespannt wird. Im nächsten Schritt werden die zwei gewählten Verfahren näher erläutert. Das erste, die *improved generalized Steinmetz equation (iGSE)*, ist ein auf der Steinmetzformel beruhender Ansatz. Dieser benötigt nur die Steinmetzparameter, die sich leicht aus den Verlustkurven im Datenblatt bestimmen lassen. Das zweite Verfahren, das *loss surface* Verfahren, bestimmt die Verluste mit Hilfe einer Oberfläche im $B\text{-}\frac{dB}{dt}$ Raum welche das Materialverhalten repräsentiert. Diese Oberfläche muss messtechnisch aufgenommen werden. Somit ist diese Methode etwas aufwändiger als die iGSE, kann allerdings auch für Materialien eingesetzt werden, für die kein Datenblatt vorhanden ist oder deren Eigenschaften durch die Bearbeitung verändert wurden.

Anschließend werden die zwei implementierten Verfahren mit verschiedenen Flussdichteverläufen messtechnisch überprüft und miteinander verglichen. Abschließend werden noch die zukünftigen Schritte, um die Genauigkeit und Anwendbarkeit der Modelle zu verbessern, diskutiert.

Chapter 1

Short overview of iron loss models

1.1 Introduction

In more and more applications of daily life small scale drives are used. Whereby the trend towards permanent magnet brushless direct current drives, so called BLDC-drives, is increasing. Domestic appliances, fans, small pumps and actuators in automobiles are only a few areas of usage. Since the number of applications is rising, the number of BLDC- drives is also rising and due to the increasing environmental awareness of the customers, an increase in efficiency of these drives is essential. Copper losses and iron losses are the two biggest losses in such machines [1]. The copper losses are relatively easy to calculate with $P_{Cu} = I^2 \cdot R_{Cu}$, when the frequency is so low that high frequency effects can be neglected. The estimation of the iron losses needs a little more effort. The aim of this thesis is to identify and implement iron loss calculation methods, which seem suitable for small scale drives and have a good trade off between accuracy and complexity. In this section a brief description of the considered iron loss models is given. Iron loss calculation is an important part of the efficiency enhancement of electric drives. Hence many teams in the world are involved in the enormous research effort, so the results are constantly changing. Therefore, this overview does not claim completeness.

1.2 Steinmetz based models

Charles Proteus Steinmetz presented his work on the calculation of losses in magnetic materials 1892 at a meeting of the American Institute of Engineers (AIEE) in New

York. From this empirical formula the losses per unite volume are calculated [2]:

$$p_v = \eta \hat{B}^{1.6}. \quad (1.1)$$

p_v ... losses during a complete cycle of magnetization
 η ... material constant
 \hat{B} ... peak value of the flux density

(1.1) does not contain any frequency dependence. However to honour his fundamental work on iron losses, (1.2) the currently used equation has been named after Steinmetz

$$p_v = k f^\alpha \hat{B}^\beta. \quad (1.2)$$

k, α and β ... material constants - Steinmetz parameters
 f ... frequency of magnetization

(1.2) is only valid for sinusoidal excitation and a limited frequency and flux density range. In modern applications the occurring flux distribution is far from sinusoidal. Due its simplicity it would be desirable to find a way how to use a form of this equation applicable to non sinusoidal waveforms. Many different Steinmetz based approaches have been developed in the past, but there a two things they all have in common.

- The Steinmetz parameters are for use in the SI- system, so the frequency must be used in Hz and the flux density in T, the calculated iron losses are in $\frac{W}{m^3}$.
- The hysteresis curve is getting wider with increasing frequency, so also the losses increase. The parameter alpha tries to describe this circumstance, but this only works for a limited frequency range. Therefore, the choice of the parameter set has big influence on the result and so one set should be only used for a certain frequency range, such as it is done in Section 2.5.

1.2.1 Modified Steinmetz Equation - MSE

A first approach to calculate core losses caused by non sinusoidal waveforms is the so called "Modified Steinmetz Equation". In [3], based on the work of Walter Röcker, et al., it was shown that the losses depend rather on $\frac{dM}{dt}$ than on the frequency of the externally applied field, where $\frac{dM}{dt}$ is the rate of change of the magnetization and so it is proportional to $\frac{dB}{dt}$. In [4] Dürnbaum introduces a method to calculate an equivalent frequency f_{eq} for an arbitrary waveform. The sinusoidal flux distribution with f_{eq} produces the same losses than the considered signal. With the normalization constant $\frac{2}{(\Delta B\pi)^2}$ the equivalent frequency can be calculated as follows [5]

$$f_{eq} = \frac{2}{(\Delta B\pi)^2} \int_0^T \left(\frac{dB}{dt} \right)^2 dt. \quad (1.3)$$

f_{eq} ... equivalent frequency

To use this frequency in the Steinmetz equation, it has to be adapted. In its original form it calculates a power loss per unit volume, if both sides are multiplied with the period duration, the energy dissipated in a complete cycle of magnetization is obtained.

$$T = \frac{1}{f} \quad (1.4)$$

$$e_v = p_v T = p_v \frac{1}{f} = k f^\alpha \frac{1}{f} \hat{B}^\beta = k f^{\alpha-1} \hat{B}^\beta \quad (1.5)$$

(1.5) calculates an energy, with the magnetization rate it becomes a power again

$$p_v = (k f_{eq}^{\alpha-1} \hat{B}^\beta) f_r. \quad (1.6)$$

f_r ... magnetization frequency

With the Modified Steinmetz Equation a simple approach is given for iron loss calculation with an arbitrary flux density waveform. The drawback of this method

is, that in most cases, the calculated iron losses are too small and the lack in accuracy rises with increasing amplitude of higher harmonics. In addition, the losses are a discontinuous function of a continuous change of the waveform parameters [6].

1.2.2 Generalized Steinmetz Equation - GSE

The "Generalized Steinmetz Equation" was developed under the assumption, that the losses are a single valued function of the instant flux density $B(t)$ and the rate of change $\frac{dB(t)}{dt}$

$$p_v = f\left(\frac{dB(t)}{dt}, B(t)\right). \quad (1.7)$$

With the help of the GSE the instantaneous losses can be calculated as follows

$$p_v(t) = k_1 \left| \frac{dB(t)}{dt} \right|^\alpha |B(t)|^{\beta-\alpha}. \quad (1.8)$$

Here k_1 differs from the constant used in the before mentioned forms of the Steinmetz equation and can be expressed as

$$k_1 = \frac{k}{(2\pi)^{\alpha-1} \int_0^{2\pi} |\cos(\Theta)|^\alpha |\sin(\Theta)|^{\beta-1} d\Theta}. \quad (1.9)$$

The mean value over the time period T is

$$\bar{p}_v = \frac{1}{T} \int_T k_1 \left| \frac{dB(t)}{dt} \right|^\alpha |B(t)|^{\beta-\alpha} dt. \quad (1.10)$$

This form of the Steinmetz equation would not work when $\alpha > \beta$, because the iron losses would get infinite. For some materials α could get larger than β , so (1.10) can not be used for these materials [7]. The assumption that the losses only depend on instantaneous values of the flux density ignores the time history of the flux density waveform and could cause reasons for inaccuracy. The iGSE tries to overcome this drawback, by considering not only instantaneous values [6].

1.2.3 improved Generalized Steinmetz Equation - iGSE

By using ΔB instead of $B(t)$ (1.10) becomes [6]

$$\bar{p}_v = \frac{1}{T} \int_T k_i \left| \frac{dB(t)}{dt} \right|^\alpha (\Delta B)^{\beta-\alpha} dt. \quad (1.11)$$

The factor k_i can be determined from the Steinmetz parameters with

$$k_i = \frac{k}{(2\pi)^{\alpha-1} \int_0^{2\pi} |\cos(\Theta)|^\alpha 2^{\beta-\alpha} d\Theta}. \quad (1.12)$$

A further increase in accuracy is achieved by decomposing the flux density waveform in one major loop and a number of minor loops, corresponding to the waveform. The flux density distribution has not to include minor loops, for a detailed description see Section 2.2. Then, the losses for every single loop are calculated with (1.11). The total losses are given by the weighted sum of the single loops

$$\bar{p}_{\text{tot}} = \sum_i \bar{p}_i \frac{T_i}{T}. \quad (1.13)$$

1.2.4 Natural Steinmetz Extension - NSE

This is a very similar approach to the iGSE and was developed by a different team at the same time. The losses, averaged over one period, can be calculated with [8]

$$\bar{p}_v = \left(\frac{\Delta B}{2} \right)^{\beta-\alpha} \frac{k_N}{T} \int_0^T \left| \frac{dB}{dt} \right|^\alpha dt. \quad (1.14)$$

The constant k_N is given by

$$k_N = \frac{k}{(2\pi)^{\alpha-1} \int_0^{2\pi} |\cos(\Theta)|^\alpha d\Theta}. \quad (1.15)$$

The main application area for the NSE are triangular flux density wave forms, as they appear very often with rectangular switching processes in power electronics [9]. Such a flux density waveform has no minor loops, see Section 2.2. Thus the decomposition of the waveform is omitted.

1.2.5 improved improved Generalized Steinmetz Equation - i^2 GSE

Referring to the iGSE, in sections of the flux density waveform with constant flux, the iron losses should be zero, because the $\frac{dB}{dt}$ - term gets zero, see Figure 1.1. Measurements have shown that this is not true and with increasing frequency of the flux density waveform the error increases too. In [10] this effect is linked with a so called relaxation processes. The H - and the B fields are shifted in time, thus if the externally applied field on a specimen has become constant, in the specimen domain wall movements and other processes are going on, to reach the new equilibrium. In this time the domain walls are moving in such a way that they occupy the state of the lowest energy. Through this movement losses occur, although the applied field is not changing any more. The movement of the domain walls is only one process which leads to the described losses, an exhaustive consideration would be misplaced here and the interested reader is referred to [11] or [12]. To take these losses into account, the iGSE is expanded by one term, the so called excess loss term [10]

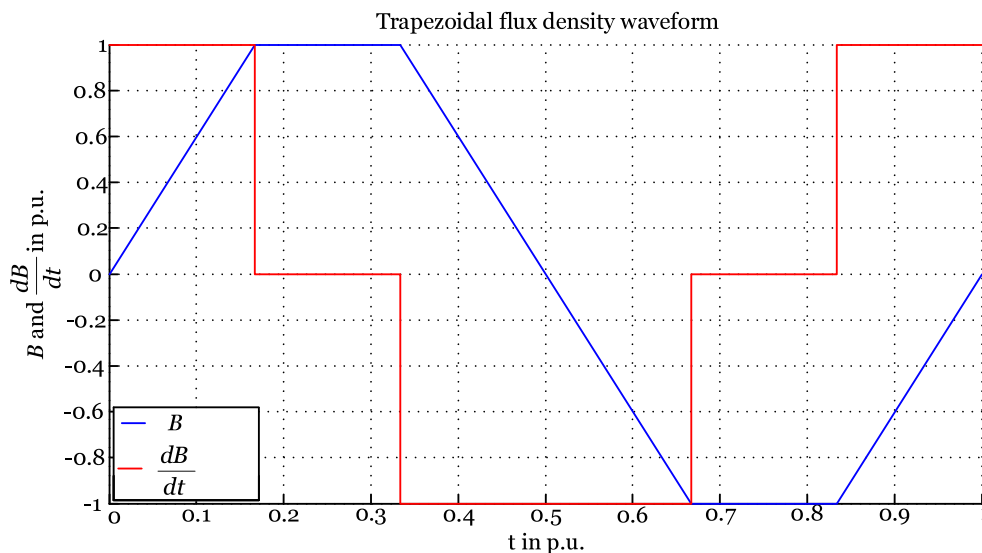


Figure 1.1: Trapezoidal flux density and its time derivative.

$$\bar{p}_v = \frac{1}{T} \int_0^T k_i \left| \frac{dB}{dt} \right|^\alpha (\Delta B)^{\beta-\alpha} dt + \underbrace{\sum_{l=1}^n p_{r,l}}_{\text{Excess loss term}} \quad (1.16)$$

$$p_{r,l} = \frac{1}{T} k_r \left| \frac{dB(t_-)}{dt} \right|^{\alpha_r} (\Delta B)^{\beta_r} \left(1 - e^{-\frac{t_1}{\tau}} \right). \quad (1.17)$$

- $p_{r,l}$... losses caused by the relaxation processes
- k_r, α_r and β_r ... material constants
- $\frac{dB(t_-)}{dt}$... derivation of the flux density before the switching
- τ ... time constant for the relaxation process
- n ... number of phases with constant flux
- t_1 ... duration of the phase with constant flux

k_r, α_r, β_r and τ are material constants which have to be determined by additional measurements. Note that these parameters are not identical to the normal Steinmetz parameters. k_i is calculated as for the iGSE, with (1.12). The relaxation processes can be described with an e- function and so the losses do not increase remarkably even if $t_1 > 5\tau$ is valid. For low frequencies the relaxation processes can be neglected, so the i²GSE is mainly used in power electronic applications.

1.2.6 Other Steinmetz based methods

Other Steinmetz based methods have been presented in the literature, many of them only apply for a special case. Others use correction factors to take influences such as higher harmonics or saturation into account and hence require very accurate knowledge of the system and a higher data input. Therefore, they are not considered here.

1.3 Loss surface model

This approach assumes that the material behaviour is exactly known if B and $\frac{dB}{dt}$ are known. Therefore, a surface in the B - $\frac{dB}{dt}$ room is derived from measurements. Both H or $H\frac{dB}{dt}$ (the instantaneous losses) can be described from this surface. To generate the surface, measurements with an Epstein frame, or with toroidal specimens and a measurement bank as described in [13], are necessary. A good choice for the flux density waveform, with which the measurements are taken, are triangular ones, because they have a constant $\left|\frac{dB}{dt}\right|$. Therefore, every measurement with a certain frequency provides values for a fixed positive and negative constant $\frac{dB}{dt}$. For the evaluation of the measurement data, either the whole or the half surface could be considered, by evaluating the whole curve or only the ascending or descending branches, because (1.18) is valid [14]

$$p_v\left(B(t), \frac{dB(t)}{dt}\right) = p_v\left(-B(t), -\frac{dB(t)}{dt}\right). \quad (1.18)$$

When (1.18) is used, the size of the file in which the loss surface is stored, is halved. Also the computational time for the calculation of the iron losses could be reduced, depending on the interpolation method used. In [15] and [16] the described surface represents the field strength H for every $B(t)$ - $\frac{dB(t)}{dt}$ data pair. With this information hysteresis loops can be generated and then the losses per magnetization cycle can be calculated. If a power should be calculated, the iron loss energy has to be divide by the time needed for one magnetization cycle. This procedure has the advantage that no parameters are required from manufacturer and for a wide flux density and frequency range data are available. In addition even the degradation of the material, due to the cutting process which changes the parameters, can be taken into account, if specimens widths are chosen to catch structures in the final application. This advantages comes with the prices of the measurements which has to be carried out by the user himself.

1.4 Loss separation approach

In [17], as cited in [9] or in [18], Jordan introduced the loss separation approach. He divided the losses in hysteresis loss term and a eddy current loss term

$$p_v = p_h + p_e = k_h \hat{B}^2 + k_e (f \hat{B})^2. \quad (1.19)$$

p_h ... hysteresis losses
 p_e ... eddy current losses
 k_h and k_e ... material constants

This simply approach delivers inadequate results for contemporary applications with novel materials, but based on this work, Bertotti expanded the formula with the so called excess loss term [19]. With it he tried to take the difference between the experiments and the forecast into account

$$p_v = p_h + p_e + p_{ex} = k_h f \hat{B}^2 + k_e (f \hat{B})^2 + k_{ex} (f \hat{B})^{\frac{3}{2}}. \quad (1.20)$$

p_{ex} ... excess losses
 k_{ex} ... material constant

If (1.20) is divided by the frequency f it becomes

$$\frac{p_v}{f} = w_v = w_h + w_e + w_{ex} = k_h \hat{B}^2 + k_e \hat{B}^2 f + k_{ex} \hat{B}^{\frac{3}{2}} f^{\frac{1}{2}} \quad (1.21)$$

and so it describes the single losses which occur for one period of the flux density B with the frequency f . The evolution of the single losses as a function of the frequency is shown in Figure 1.2 [20].

With increasing frequency the hysteresis losses stay constant, but the dynamic losses, the sum of the eddy current and excess losses, increase. This fact must be considered in applications where the iron is exposed to flux densities with high frequencies. Such it is the case when frequency inverters are used or where the flux density has a high content of harmonics because it is not sinusoidal anymore.

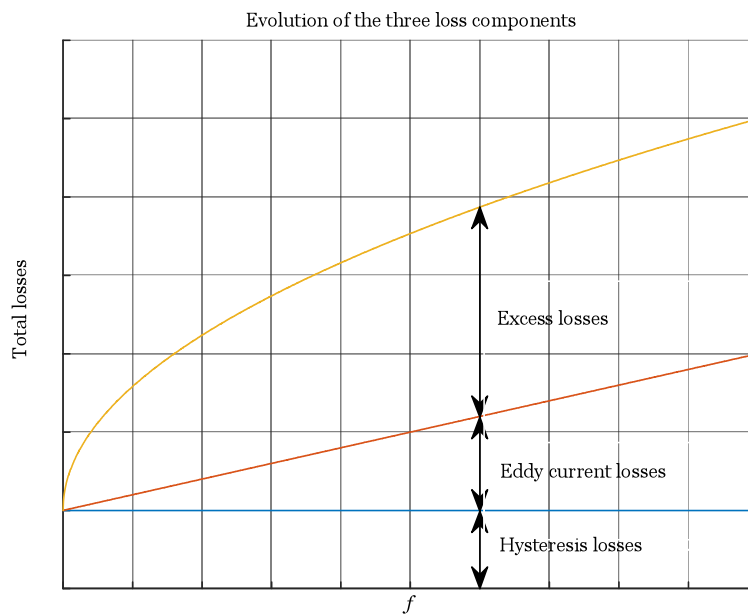


Figure 1.2: Single losses as a function of the frequency [20].

1.5 Physically based methods

Beside the empirical approaches, which are mainly used for engineering purposes, also physically based approaches have been developed. These models are able to describe the material behaviour very well, but with increasing accuracy also the calculation time increases and in most cases they use more parameters than the empirical ones. One thing they have in common is that they describe the hysteresis loop in a mathematical way. So they try to reproduce the hysteresis behaviour. The losses which arise during the change of magnetization could be calculated with the BH integral

$$e_h = \int HdB. \quad (1.22)$$

This integral equals the enclosed area of the hysteresis loop and has the dimension of energy per volume. The power loss is calculated by multiplying (1.22) with the frequency of magnetization

$$p_v = f_r \int HdB. \quad (1.23)$$

1.5.1 Preisach model

This model was published in 1935 by F. Preisach [21]. The principle is based on the representation of the complex form of the hysteresis loop by the weighted superposition of many so called Preisach hysterons (HR). Figure 1.3 shows the relationship between the in- and output of such a hysteron. The output can only be -1 or 1 respectively. If the upper switching threshold α is exceeded from a level below α , the output takes the high state. If the input falls below the lower switching threshold β , the output takes the low state. If the input is in between the two switching thresholds, the output retains its previous state.

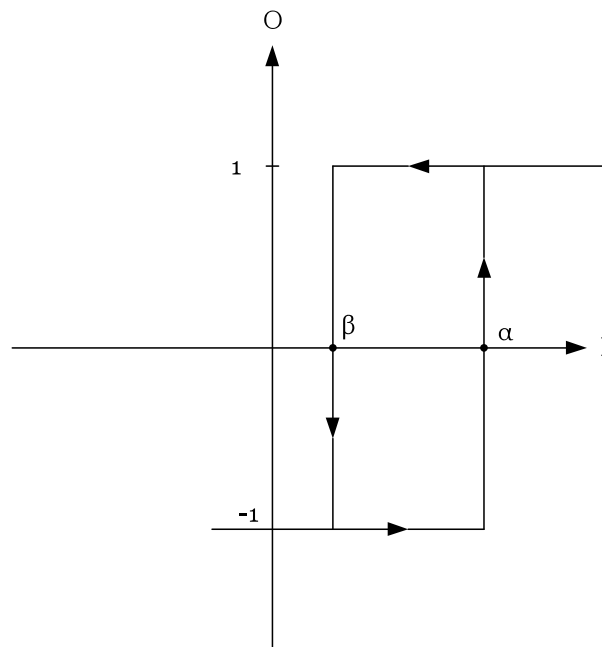


Figure 1.3: Hysteron with the switching thresholds α and β .

By parallel connecting many hysterons and weighting their outputs, the magnetic behaviour of the material is described.

Each hysteron has its own switching thresholds. The function, which calculates the weighting factors $\mu_x(\alpha_x, \beta_x)$, is called weighting function or Preisach function. With an increasing number of hysterons the loss behaviour can be described with increasing accuracy, when n finally goes to infinity, the discrete hysteresis loop becomes a continuous one. The output of the whole system can be determined by

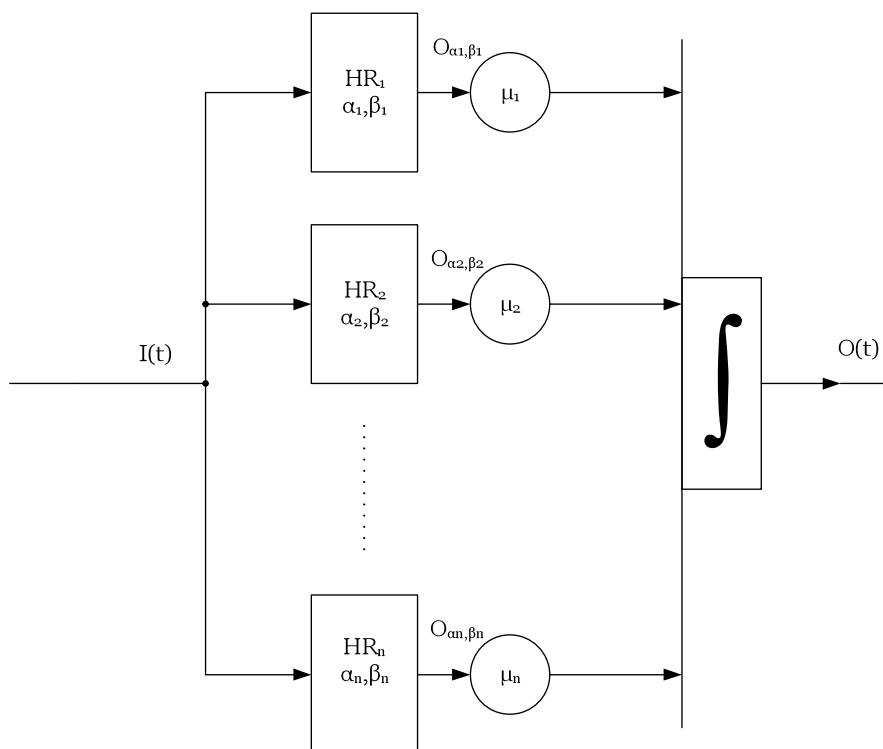


Figure 1.4: Parallel connection of single hysterons [21].

the integral

$$O(t) = \int \int_{\alpha \geq \beta} \mu(\alpha, \beta) O_{\alpha, \beta}(t_0, n_0) I(t) d\alpha d\beta. \quad (1.24)$$

The Preisach model is able to describe also other systems where hysteresis is involved, so in Figure 1.4 the input is called $I(t)$ and the output $O(t)$ respectively. Considering magnetic systems, the input is the magnetic field and the output the magnetization of the material. The model considered until now only describes static hysteresis, the rate of change is neglected. Some Preisach based approaches to include the changing behaviour for higher frequencies, have been proposed in literature such as [21] or [22].

One approach, as shown in [21], is to introduce a dependency of the weighting function $\mu(\alpha, \beta)$ on the rate of change of the output $\frac{dO(t)}{dt}$. So 1.24 gets

$$O(t) = \int \int_{\alpha \geq \beta} \mu\left(\alpha, \beta, \frac{dO(t)}{dt}\right) O_{\alpha, \beta}(t_0, n_0) I(t) d\alpha d\beta. \quad (1.25)$$

1.5.2 Jiles Atherton model

This model describes the material behaviour with a differential equation, where a Langevin function is used. This special function has the form as shown in (1.26)

$$L(x) = \coth(x) - \frac{1}{x}. \quad (1.26)$$

The anhysteretic magnetization is the magnetization which occurs when the material shows no hysteresis behaviour and can be described by the so called initial magnetisation curve. This special waveform can be approximated with the Langevin function [23]. The differential equation to calculate the magnetization is stated below [24]

$$M_{\text{an}} = M_s \left[\coth\left(\frac{H + \alpha M}{a}\right) - \frac{a}{H + \alpha M} \right] \quad (1.27)$$

$$\frac{dM}{dH} = (1 - c) \frac{M_{\text{an}} - M}{k\delta - \alpha(M_{\text{an}} - M)} + c \frac{dM_{\text{an}}}{dH}. \quad (1.28)$$

- M_{an} ... anhysteretic magnetization
 M_s ... saturation magnetization
 a, α, c and k ... material parameters

The material parameters a and α influence the shape of the hysteresis loop, k and c affect the width and M_s the height. δ is the $\text{sign}\left(\frac{dH}{dt}\right)$ function, it distinguishes between the ascending branch ($\text{sign}\left(\frac{dH}{dt}\right) = 1$) and the descending branch ($\text{sign}\left(\frac{dH}{dt}\right) = -1$) [25]. The Jiles Atherton model in this form can lead to insufficient results when distorted hysteresis loops (asymmetrical excitation) are involved. In [24] a procedure is shown how to expand the Jiles Atherton model in such a way that also the distorted hysteresis loops and the changing behaviour with increasing frequency can be taken into account. The approach is to express the single parameters as a function of the magnetic field. This can be done in different ways, the relationship between the parameters and the magnetic field can be a linear one, a gaussian one or as in [24] a combination of a constant and a excitation dependent factor. The drawback of the approach in [24] is that, ten instead of five parameters have to be determined, but it delivers accurate results.

1.6 Conclusion

In this chapter a short overview of the considered iron loss models was given. These includes simple empirical approaches, such as the Steinmetz based ones, as well as complex physical models, e.g., the expanded Jiles Atherton model from [24], where ten parameters have to be determined. For a more comprehensive overview, reference is made to [9]. Special attention has to be paid on calculation time and the effort for the determination of the parameters. Thus, for this work FEM based methods and magnetic circuit methods are not considered. Although the literature research was performed thorough, it was not possible to find anything suitable which complies with the requirements for complex waveforms and the possibility to consider the processing of the used iron in fractional horse power motors. So the iGSE and the loss surface approach were chosen. Both methods are able to deal with complex waveforms as they appear with BLDC- drives. The iGSE is a simple model which only needs the parameters from the data sheet of the used material. The loss surface approach is a good choice, as it allows implicitly considering the cutting process that may alter the parameters of the data sheets and can be applied if no data sheets exist. Both with this Steinmetz based method and with the measurement based method a tool is designed and implemented for calculating the iron losses which offers advantages of other methods concerning non sinusoidal waveforms. Table 1.1 shows an overview of the different iron loss models and their characteristics, it is based mainly on the table in [9] and should give an overview about the advantages and disadvantages of the single models.

Iron loss model	Complex waveforms	Material prior knowledge	Accuracy	Literature
Steinmetz Equation	-	small	low	[2]
Modified Steinmetz Equation	+	small	low - medium	[5]
Generalized Steinmetz Equation	-	medium	low - medium	[7], [6]
Improved Generalized Steinmetz Equation	+	medium	low-medium	[6]
Natural Steinmetz Extension	+	medium	low - medium	[8]
Improved improved Generalized Steinmetz Equation	+	high	medium	[6]
Loss separation model	-	medium	medium	[17]*, [19]
Classical Preisach model	+	high	good	[21], [22]
Jiles- Atherton model	+	high	good	[25], [24]
Loss surface model	+	high	medium - good	[13], [14], [15], [16]

*:as cited in [9] or in [18]

Table 1.1: Extended version of the table in [9].

Chapter 2

Iron loss calculation with the iGSE

2.1 Introduction

In this Chapter the improved generalized Steinmetz equation (iGSE) is introduced, as the name suggests, this approach is based on the Steinmetz formula. To overcome the drawback of the original equation, that only sinusoidal flux density waveforms can be calculated, also the dependency of $\frac{dB}{dt}$ is taken into account. It is not tried to find an equivalent frequency, which causes the same losses, as it is done by the modified Steinmetz equation (MSE). The iGSE separates the flux density waveform in its main- and subloops, for every single loop the losses are calculated and in the end a weighted sum is used. Another big advantage is that this approach is only based on Steinmetz parameters, which can be estimated very easily from the loss curves provided by the manufacturer of the iron.

2.2 Nested loop algorithm

As shown in [6], the flux density over the time has to be separated in its main- and subloops. It is possible that the minorloops also contain subloops, this nesting can achieve any level, so the algorithm has to be capable to detect subloops at any nested level. To realize this separation, an algorithm was implemented in MATLAB, the fundamental principle is described in [6]. The authors of [6] provide their MATLAB code but tests with different signals showed inaccuracies, so an own version was implemented. In principle the process can be divided in the following steps

- Separation of the waveform in an ascending and a descending branch. The ascending branch reaches from the global minimum to the global maximum.

The same is valid for the descending branch, from the maximum to the minimum. If the function has more than one maximum or minimum it can be chosen freely which points are taken for the division. In general, one of the branches will not be in the waveform in one piece, one part will be at the end of the period and the other one will be at the beginning.

- Separation of the main- and subloops. A subloop in the ascending branch starts when the value of the next point is smaller than the value of the actual point. It ends when the waveform reaches the value it had before the start of the subloop. For the descending branch the subloop starts when the waveform increases. An example for a first level subloop is shown in Figure 2.1. The two subloops are plotted in red. If these are removed from the waveform the mainloop in blue remains.
- Check if the subloops contain any minor loops. If this is the case apply the first two steps on the subloops. These steps are repeated as long as there are minor loops in the subloops.

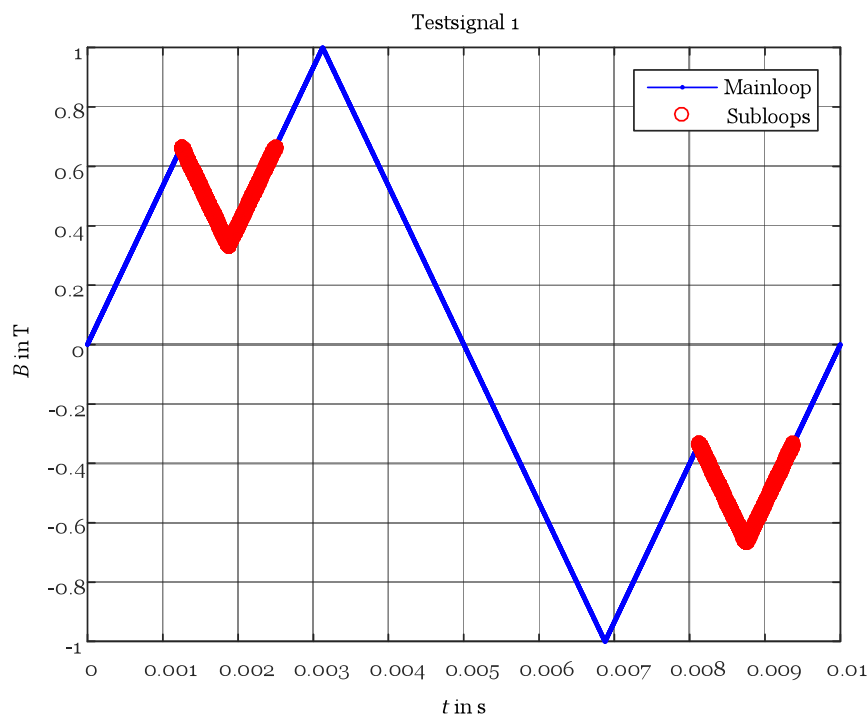


Figure 2.1: First level subloop.

An example for a second level subloop is shown in Figure 2.2. As in Figure 2.1, the mainloop is plotted in blue and the subloops, now including minor loops, are marked in red. For the sake of clarity the first level subloops and their decomposition is shown with an offset.

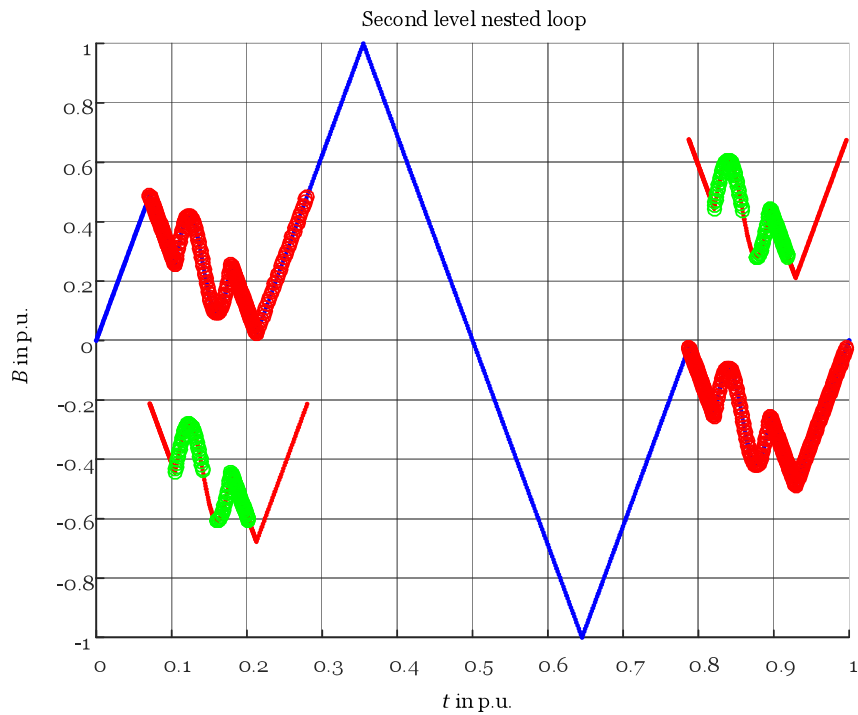


Figure 2.2: Second level subloop.

In Figure 2.3 a signal with one subloop in the rising branch and one subloop in the falling branch of the flux density waveform and their affiliation in the hysteresis loop is shown. It can be seen, that a subloop in the flux density over time leads to a minor loop in the hysteresis loop.

The user's input is verified for mistakes which could lead to errors during the calculation, but not if the input is meaningful. The iGSE is for the iron loss calculation caused by a closed hysteresis loop. So the user has to verify if the waveform of $B(t)$ represents a closed loop and only contains one period.

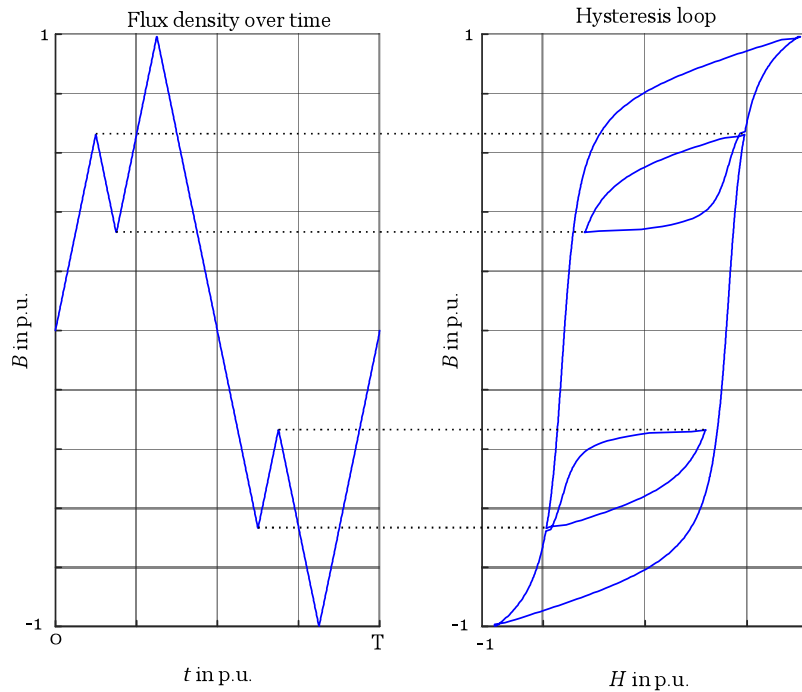


Figure 2.3: Nested loops in the hysteresis loop.

2.3 Equations

In this section the equations which are used to calculate the iron losses with the iGSE are stated. If the main- and all the subloops are separated from the waveform of the flux density, the losses caused by every single loop can be calculated with (2.1) [6]

$$\bar{p}_v = \frac{1}{T} \int_T k_i \left| \frac{dB(t)}{dt} \right|^\alpha (\Delta B)^{\beta-\alpha} dt, \quad (2.1)$$

where the factor k_i is

$$k_i = \frac{k}{(2\pi)^{\alpha-1} \int_0^{2\pi} |\cos(\Theta)|^\alpha 2^{\beta-\alpha} d\Theta}. \quad (2.2)$$

The total losses of the given waveform are obtained from the sum of every single weighted loop. The weighting factor takes into account, that the period of the single

loops is not as long as the period of the original waveform

$$\bar{p}_{\text{tot}} = \sum_i \bar{p}_i \frac{T_i}{T}. \quad (2.3)$$

2.4 Verification based on simple signals

The implemented algorithm was verified by analytic signals, because a cross check can be done by hand easily. It should be checked if the algorithm separates the main- and the subloops and if it calculates the iron losses correctly.

2.4.1 Testsignal 1 - Combined triangular signal

The first signal is shown in Figure 2.1, the frequency is 100 Hz and the amplitude 1 T. This simple signal allows it to check if the algorithm detects the subloops and calculates the iron losses right. The first subloop extends from 1.25 ms to 2.5 ms and the second one from 8.125 ms to 9.375 ms, the rest of the waveform belongs to the mainloop. If the Steinmetz parameters are known, the iron losses could be calculated. For test purposes it is assumed that the material is N87, because the parameters are known from [26]

Steinmetz parameters - N87	
α	1.25
β	2.46
k	15.9

Table 2.1: Parameters for N87 [26].

These parameters are for use in the SI- system, this must be considered in further calculations to get the right results. In Figure 2.4 the mainloop of the signal is shown.

The mainloop's period duration

$$T_{\text{main}} = 10.625 \text{ ms} - 3.125 \text{ ms} = 7.5 \text{ ms}. \quad (2.4)$$

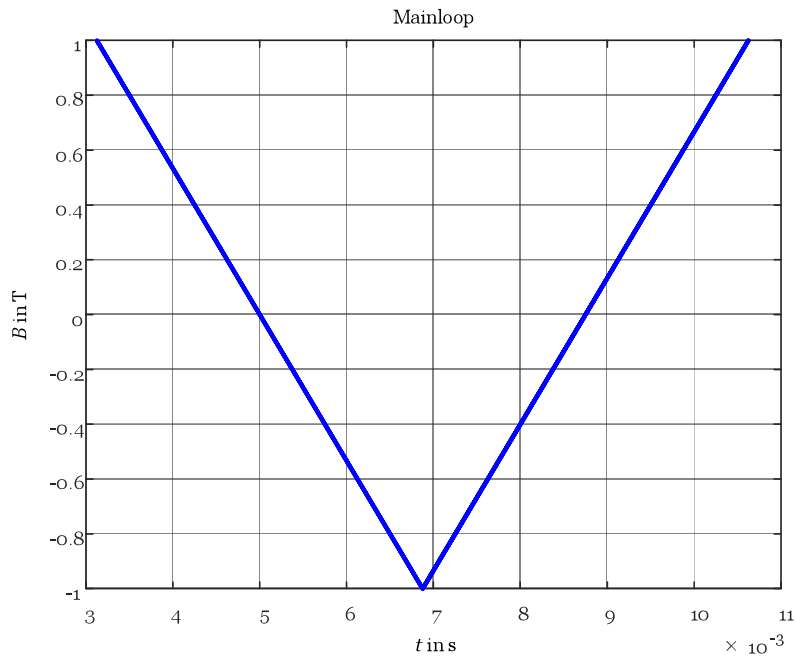


Figure 2.4: Mainloop of the test signal.

The mainloop is triangular, so $\frac{dB}{dt} = \frac{\Delta B}{\Delta t}$ is valid

$$\frac{dB_{\text{main}}}{dt} = \frac{-1 \text{ T} - 1 \text{ T}}{6.875 \text{ ms} - 3.125 \text{ ms}} = -533.3 \frac{\text{T}}{\text{s}}. \quad (2.5)$$

For the further calculation only the absolute value of $\frac{dB}{dt}$ is of interest and it is the same for the ascending and descending branch

$$\left| \frac{dB_{\text{main}}}{dt} \right| = 533.3 \frac{\text{T}}{\text{s}}. \quad (2.6)$$

To calculate the losses of the mainloop the peak to peak flux density ΔB_{main} of the mainloop and the factor k_i have to be determined

$$\Delta B_{\text{main}} = B_{\text{main, max}} - B_{\text{main, min}} = 1 \text{ T} - (-1 \text{ T}) = 2 \text{ T} \quad (2.7)$$

$$\begin{aligned}
 k_i &= \frac{k}{(2\pi)^{\alpha-1} \int_0^{2\pi} |\cos(\Theta)|^\alpha 2^{\beta-\alpha} d\Theta} = \\
 &= \frac{15.9}{(2\pi)^{1.25-1} \int_0^{2\pi} |\cos(\Theta)|^{1.25} 2^{2.46-1.25} d\Theta} = 1.1659.
 \end{aligned}
 \tag{2.8}$$

With these informations the losses caused by the mainloop can be estimated by

$$\begin{aligned}
 \bar{p}_{v, \text{main}} &= \frac{1}{T_{\text{main}}} \int_{T_{\text{main}}} k_i \left| \frac{dB(t)}{dt} \right|^\alpha (\Delta B)^{\beta-\alpha} dt = \\
 &= \frac{1}{7.5 \text{ ms}} \int_{t=0}^{7.5 \text{ ms}} 1.1659 \cdot 533.3^{1.25} \cdot 2^{2.46-1.25} dt = 6.9123 \frac{\text{kW}}{\text{m}^3}.
 \end{aligned}
 \tag{2.9}$$

Figure 2.5 shows one exemplary subloop

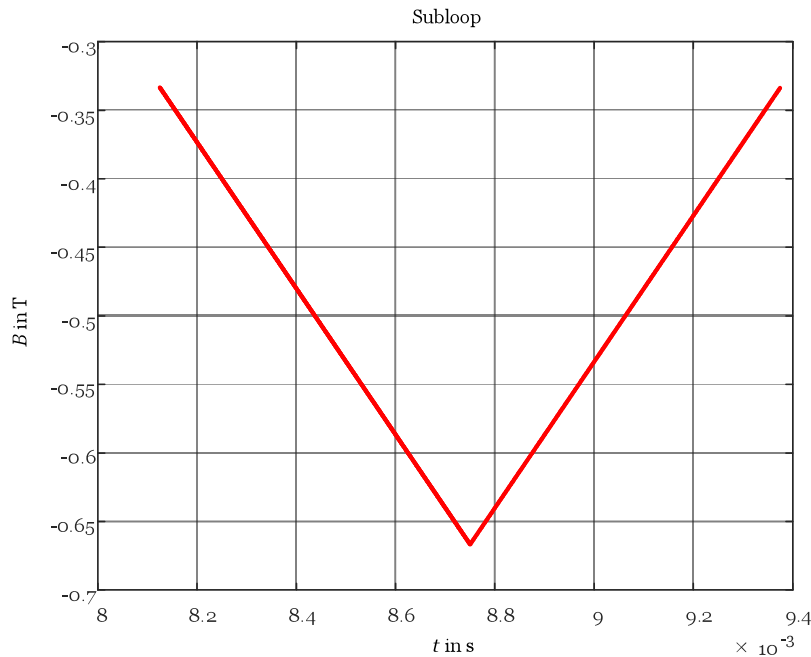


Figure 2.5: Subloop of the signal.

The durations of both subloops are equal and only the absolute value of $\frac{dB}{dt}$ is of interest, so only one subloop has to be calculated, the result can be multiplied by 2.

The procedure is the same as for the mainloop, so only the results are stated.

$$T_{\text{sub}} = 1.25 \text{ ms} \quad (2.10)$$

$$\left| \frac{dB_{\text{sub}}}{dt} \right| = 533.3 \frac{\text{T}}{\text{s}} \quad (2.11)$$

$$\Delta B_{\text{sub}} = \frac{1}{3} \text{ T} \quad (2.12)$$

$$\bar{p}_{v, \text{sub}} = 790.79 \frac{\text{W}}{\text{m}^3} \quad (2.13)$$

The contributions of the single losses are summed up to obtain the total losses

$$\begin{aligned} \bar{p}_{\text{tot}} &= \sum_i \bar{p}_i \frac{T_i}{T} = \frac{1}{10 \text{ ms}} \left(6.9123 \frac{\text{kW}}{\text{m}^3} 7.5 \text{ ms} + 2 \cdot 790.79 \frac{\text{W}}{\text{m}^3} 1.25 \text{ ms} \right) = \\ &= 5.3819 \frac{\text{kW}}{\text{m}^3}. \end{aligned} \quad (2.14)$$

Comparison	
MATLAB	analytic
5.3823 $\frac{\text{kW}}{\text{m}^3}$	5.3819 $\frac{\text{kW}}{\text{m}^3}$

Table 2.2: Comparison of the results for the first testsignal.

The difference between the two results is marginal and the error is due to rounding in the calculation by hand.

2.4.2 Testsignal 2 - Sinusoidal Signal

The previous verification was done before the Steinmetz parameters for the used material were known, so the N87 parameters were used. The next two calculations use the parameters for isovac 250-35 A, these parameters are determined in Section 2.5. The next considered signal is a sine with a frequency of 500 Hz and an amplitude of 1100 mT. This flux density waveform contains no subloops, but the losses are known from the data sheet and so it can be verified if they are calculated correctly.

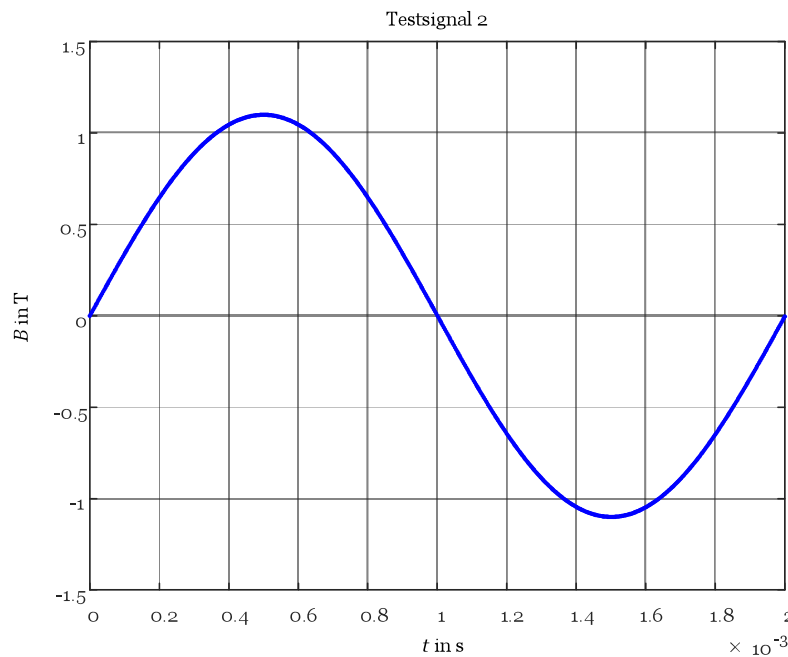


Figure 2.6: Sinusoidal signal with a frequency of 500 Hz and an amplitude of 1100 mT.

For this amplitude and frequency the following parameters are used

isovac 250-35 A parameters for 500 Hz	
k	7.9
α	1.6
β	2.6

Table 2.3: Parameters for isovac 250-35 A at 500 Hz.

The factor k_i with is given with

$$\begin{aligned}
 k_i &= \frac{k}{(2\pi)^{\alpha-1} \int_0^{2\pi} |\cos(\Theta)|^\alpha 2^{\beta-\alpha} d\Theta} = \\
 &= \frac{7.9}{(2\pi)^{1.6-1} \int_0^{2\pi} |\cos(\Theta)|^{1.6} 2^{2.6-1.6} d\Theta} = 0.3939.
 \end{aligned} \tag{2.15}$$

$B(t)$ is sinusoidal, so $\frac{dB}{dt}$ is cosinusoidal

$$\left| \frac{dB}{dt} \right| = \left| \frac{d}{dt} (1100 \text{ mT} \sin(\omega t)) \right| = |1100 \text{ mT} \cos(\omega t) \omega|. \tag{2.16}$$

With the peak to peak flux density

$$\Delta B = 2 \cdot 1100 \text{ mT} = 2200 \text{ mT} \tag{2.17}$$

the iron losses can be determined

$$\begin{aligned}
 \bar{p}_v &= \frac{1}{T} \int_T k_i \left| \frac{dB(t)}{dt} \right|^\alpha (\Delta B)^{\beta-\alpha} dt = \\
 &= \frac{1}{2 \text{ ms}} \int_{t=0}^{2 \text{ ms}} 0.3939 |1100 \cdot 10^{-3} \cos(2\pi 500 \cdot t) 2\pi 500|^{1.6} \cdot 2.2^{2.6-1.6} dt = \\
 &= 210.67 \frac{\text{kW}}{\text{m}^3}.
 \end{aligned} \tag{2.18}$$

Comparison	
MATLAB	analytic
210.85 $\frac{\text{kW}}{\text{m}^3}$	210.67 $\frac{\text{kW}}{\text{m}^3}$

Table 2.4: Comparison of the results for the second test signal in $\frac{\text{kW}}{\text{m}^3}$.

It can be seen that the difference between the result of the MATLAB program and the analytic calculation is very small and can be explained by the fact that the automated calculation uses time discrete values to approximate the flux density distribution and the Steinmetz equation is an approximation formula. To compare the calculated losses with the losses given in the data sheet, the specific losses in $\frac{\text{W}}{\text{kg}}$

have to be transferred to $\frac{W}{m^3}$. To do so the density of the material ρ is needed, it is given in the data sheet with $\rho = 7.6 \frac{g}{cm^3} = 7600 \frac{kg}{m^3}$ [27]

$$\bar{p}_{\frac{W}{kg}} = \frac{\bar{p}_{\frac{kW}{m^3}}}{\rho_{\frac{kg}{m^3}}} = \frac{210.85 \frac{kW}{m^3}}{7.6 \cdot 10^3 \frac{kg}{m^3}} = 27.74 \frac{W}{kg}. \quad (2.19)$$

Comparison	
MATLAB	Datasheet
$27.74 \frac{W}{kg}$	$27.70 \frac{W}{kg}$

Table 2.5: Comparison of the results for the second test signal in $\frac{W}{kg}$ with the data sheet [27].

A very good match of the result with the data sheet could be found. The iGSE uses the Steinmetz parameters to calculate the iron losses, due to the fact that these parameters describe only an approximation of the real flux density distribution, the results will only be as good as this approximation. Section 2.5 compares the real waveform and the approximation.

2.4.3 Testsignal 3 - Approximation of a yoke flux density

The function of the algorithm was tested with a trapezoidal flux density waveform which is often used for BLDC commutation. To calculate the waveform analytically, it was approximated by a trapezoidal one.

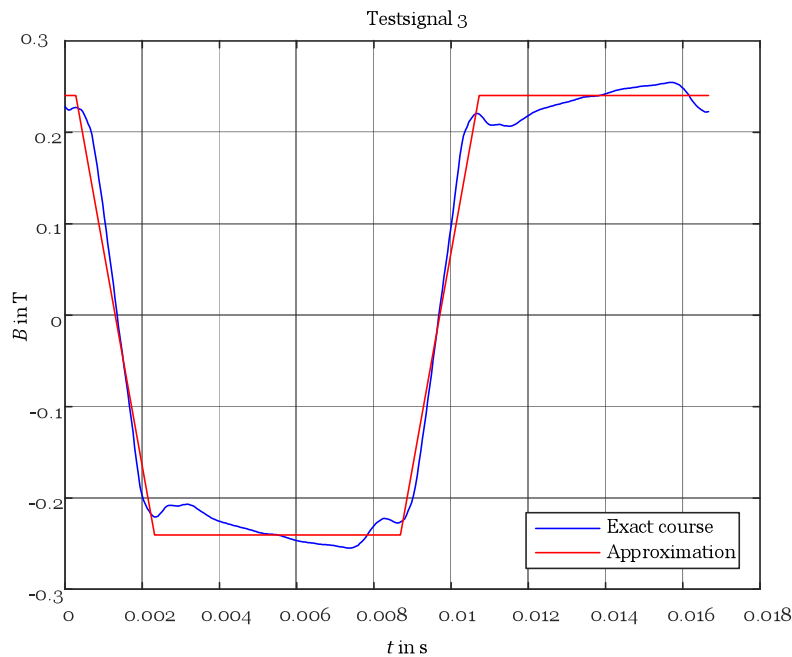


Figure 2.7: Trapezoidal approximation for the flux density in the yoke.

Due to the $\frac{dB}{dt}$ term in the loss formula of the iGSE, only the two edges of the approximated signal contribute to the iron losses, the slope for the ascending and the descending branch is the same

$$\left| \frac{dB}{dt} \right| = \left| \frac{-0.2406T - 0.2406T}{23.15 \cdot 10^{-4}s - 2.778 \cdot 10^{-4}s} \right| = 236.21 \frac{T}{s}. \quad (2.20)$$

ΔB is given with

$$\Delta B = 0.2406 T - (-0.2406 T) = 0.4812 T. \quad (2.21)$$

The duration of the signal is

$$T = 0.01667 s. \quad (2.22)$$

This period equals a frequency of approximately 60 Hz, so the parameters of Table 2.6 were used

isovac 250-35 A parameters for 60 Hz	
k	43.5
α	1.3
β	2.1

Table 2.6: Parameters for isovac 250-35 A at 60 Hz

The duration of the mainloop is

$$T_{\text{main}} = 40.744 \cdot 10^{-4} \text{ s.} \quad (2.23)$$

The factor k_i is given with

$$\begin{aligned} k_i &= \frac{k}{(2\pi)^{\alpha-1} \int_0^{2\pi} |\cos(\Theta)|^\alpha 2^{\beta-\alpha} d\Theta} = \\ &= \frac{43.5}{(2\pi)^{1.3-1} \int_0^{2\pi} |\cos(\Theta)|^{1.3} 2^{2.1-1.3} d\Theta} = 3.92. \end{aligned} \quad (2.24)$$

With (2.2)

$$\begin{aligned} \bar{p}_v &= \frac{1}{T} \int_T k_i \left| \frac{dB(t)}{dt} \right|^\alpha (\Delta B)^{\beta-\alpha} dt = \\ &= \frac{1}{40.744 \cdot 10^{-4} \text{ s}} \int_{t=0}^{40.744 \cdot 10^{-4} \text{ s}} 3.92 \cdot 236.21^{1.3} \cdot 0.4812^{2.1-1.3} dt = \\ &= 2657.26 \frac{\text{W}}{\text{m}^3} \end{aligned} \quad (2.25)$$

and (2.3) the total losses are

$$\bar{p}_{\text{tot}} = \sum_i \bar{p}_i \frac{T_i}{T} = \frac{40.744 \cdot 10^{-4} \text{ s}}{0.01667 \text{ s}} \cdot 2657.26 \frac{\text{W}}{\text{m}^3} = 649.475 \frac{\text{W}}{\text{m}^3}. \quad (2.26)$$

Comparison		
approximation - MATLAB	approximation - analytic	exact waveform - MATLAB
649.19 $\frac{W}{m^3}$	649.48 $\frac{W}{m^3}$	702.58 $\frac{W}{m^3}$

Table 2.7: Comparison of the results for testsignal 3.

As shown in Table 2.7, the losses calculated with MATLAB and the losses calculated analytically, fit very well. Additionally to the two results for the approximated curve, the result of the implemented MATLAB algorithm and the exact waveform is shown. With an error of about 8%, the result of the approximation is in the same range as the exact curve. Of course a smaller error would be preferable, but the approximation should not deliver exact results, it only should proof the plausibility of the MATLAB algorithm.

2.5 Brute force parameter fit

To apply Steinmetz based methods the Steinmetz parameters have to be known. The considered drives are all made of the electrical steel isovac 250-35 A from voestalpine. In the data sheet only the losses over the magnetic polarisation of the material, for different sinusoidal excitations at different frequencies, are given, so the parameters have to be determined. The Steinmetz parameters vary with frequency and flux density and are not stated. So if the Steinmetz parameters are of interest, the user has to determine them by himself with the relevant data from the data sheet. Because only one sort of electric steel is used, no great effort was made to make the algorithm for the determination of the parameters very efficient. A simple brute force algorithm was used, which searches for the best set of parameters over a wide range. The following table shows an excerpt of the data sheet for a frequency of 60Hz.

60 Hz				
<i>Nr.</i>	<i>J</i>	<i>H</i>	<i>P_s</i>	<i>μ_r</i>
-	mT	$\frac{A}{m}$	$\frac{W}{kg}$	-
1	600	47	0.44	10911
2	650	50	0.51	11145
3	700	53	0.58	11294

Table 2.8: Excerpt of the table for 60 Hz from the data sheet [27].

Such a table is given in the data sheet for frequencies of 50, 60, 200, 400, 500, 600, 700, 800 and 1000 Hz. Based on these data, one set of parameters was generated for every single frequency. To use the data from the data sheet they have to be adapted, because the losses are given in $\frac{W}{kg}$ and the Steinmetz equation calculates the losses in $\frac{W}{m^3}$. The density of the material is given with $\rho = 7.60 \frac{g}{cm^3} = 7600 \frac{kg}{m^3}$, so

$$\bar{p}_{\frac{W}{m^3}} = \frac{\bar{p}_{\frac{W}{kg}}}{\rho_{\frac{kg}{m^3}}}. \quad (2.27)$$

The Steinmetz equation uses the flux density and not the given magnetic polarisation. The flux density and the polarisation are linked via

$$B = \mu_0 H + J. \quad (2.28)$$

- B* ... magnetic flux density in the material
- μ_0 ... vacuum permeability
- H* ... magnetic field strength
- J* ... magnetic polarisation of the material

The Steinmetz parameters determined via the brute force algorithm, for the different frequencies, are stated in Table 2.9

One set of parameters per frequency				
Nr.	f	k	α	β
-	Hz	-	-	-
1	50	43.4	1.3	2.1
2	60	43.5	1.3	2.1
3	200	42.5	1.3	2.4
4	400	27	1.4	2.5
5	500	7.9	1.6	2.6
6	600	31.4	1.4	2.2
7	700	31.9	1.4	2.3
8	800	32.5	1.4	2.4
9	1000	35.4	1.4	2.4

Table 2.9: One set of Steinmetz parameters per frequency.

In Figure 2.8 the waveforms achieved by the parameters and the Steinmetz equation are compared to the data from the data sheet.

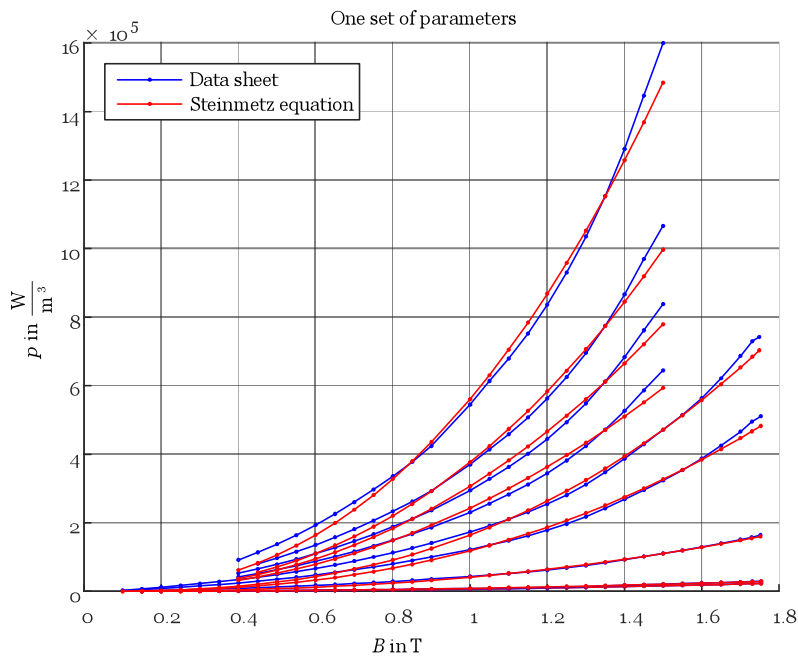


Figure 2.8: Comparison with one set of Steinmetz parameters.

As can be seen, the match, especially at low and high flux densities, is not very good. To obtain better results the flux density range of every frequency is divided to three equidistant parts, for every part an own set of Steinmetz parameters is determined, providing three sets of parameters for one frequency. Table 2.10 shows the results.

In Figure 2.9 the waveforms which are achieved with three sets of parameters per frequency and the Steinmetz equation are shown.

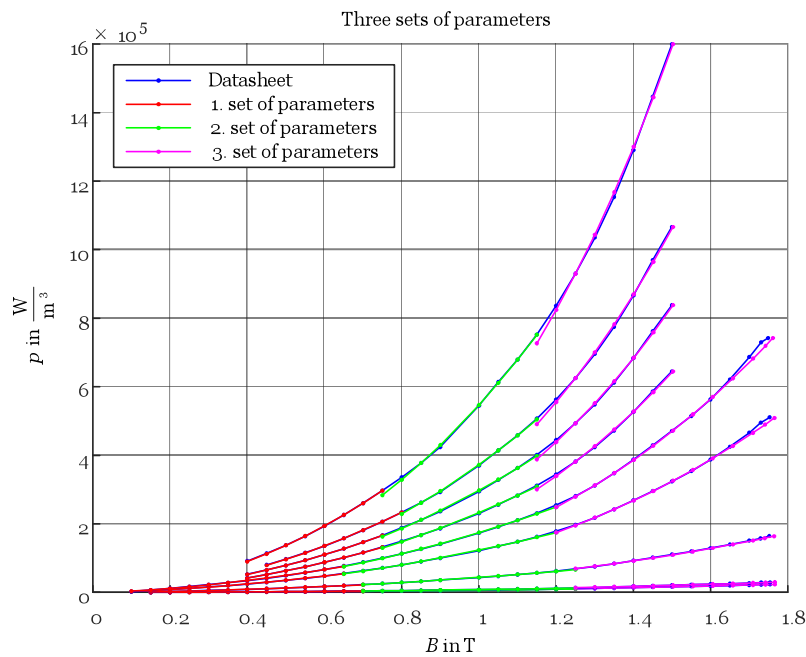


Figure 2.9: Comparison with three sets of Steinmetz parameters.

Three sets of parameters per frequency				
f	B	k	α	β
Hz	T	-	-	-
50	0.15 - 0.7001	25.2	1.4	1.6
	0.7001 - 1.2502	27.3	1.4	1.9
	1.2502 - 1.7666	28	1.4	2.2
60	0.15 - 0.7001	37.3	1.3	1.6
	0.7001 - 1.2502	40.4	1.3	1.9
	1.2502 - 1.7666	27.5	1.4	2.2
200	0.15 - 0.7001	14	1.5	1.6
	0.7001 - 1.2502	44.7	1.3	1.9
	1.2502 - 1.7646	40.5	1.3	2.5
400	0.1 - 0.6501	13.5	1.5	1.6
	0.6501 - 1.2002	28.1	1.4	1.9
	1.2002 - 1.7656	43.1	1.3	2.8
500	0.1 - 0.6501	47	1.3	1.6
	0.6501 - 1.2002	8.4	1.6	2
	1.2002 - 1.7616	13.5	1.5	2.8
600	0.4001 - 0.7501	28.5	1.4	1.8
	0.7501 - 1.1502	30	1.4	2
	1.1502 - 1.5029	3.9	1.7	2.8
700	0.4001 - 0.7501	28.8	1.4	1.8
	0.7501 - 1.1502	30.9	1.4	2.1
	1.1502 - 1.5028	13.9	1.5	2.9
800	0.4501 - 0.8002	15.8	1.5	1.9
	0.8002 - 1.1503	32.1	1.4	2.2
	1.1503 - 1.5028	3.8	1.7	2.9
1000	0.4001 - 0.7502	32.4	1.4	1.9
	0.7502 - 1.1503	17.4	1.5	2.2
	1.1503 - 1.5028	15.5	1.5	2.9

Table 2.10: Three sets of Steinmetz parameters per frequency.

Figure 2.10 shows the comparison of the results with one set of parameters, three sets of parameters and the curve of the data sheet at a frequency of 700 Hz.

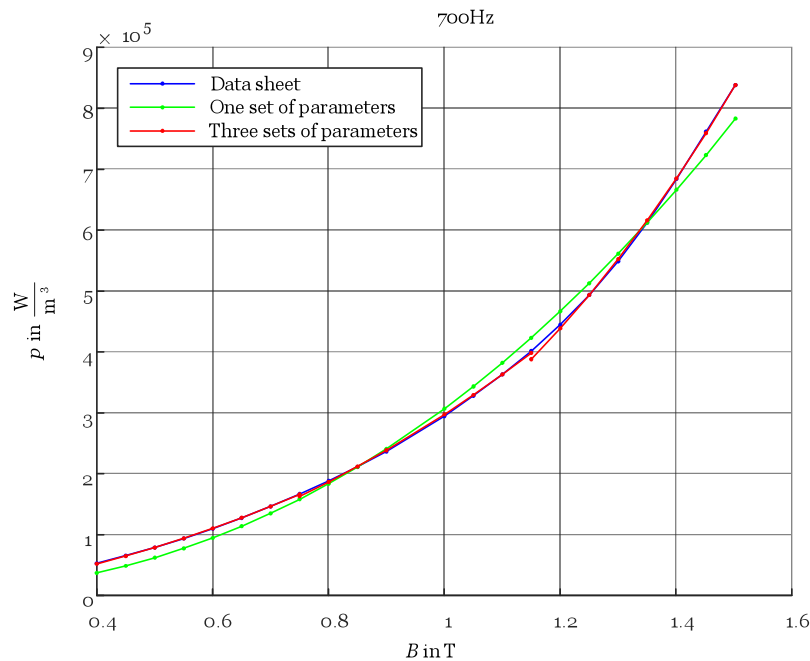


Figure 2.10: Comparison at 700 Hz.

2.6 Conclusion

The iGSE is a Steinmetz based method, so only the Steinmetz parameters and the flux density distribution are needed. The parameters can be determined very easily from the values from the data sheet, so no measurements are necessary for the application of these iron loss calculation method. A further increase to accuracy was achieved by dividing the flux density range of every frequency in three equidistantly parts. The nested loop algorithm works well and does detect subloops. In Chapter 4 the measured iron losses and the result of the iGSE are compared. This comparison shows a quiet good agreement of the predicted losses and the measurements.

Chapter 3

Loss surface model

3.1 Introduction

In this chapter the second procedure for iron loss calculation is introduced. Many works have discussed this theme, such as [16], [14], [15], [28], [29] and [30]. The approaches respectively the applications differ slightly from each other. For example in [15] and [16] the losses are separated in a static and a dynamic part. The static contribution can be modelled with any static hysteresis model, whereas the dynamic losses are modelled with the loss surface. [14] and [30] describe the whole behaviour of the material with the loss surface, eliminating the need for a static hysteresis model. Another distinctive feature is the physical quantity, which is represented by the z -axis. It can be used for the field strength H or the instantaneous specific losses p_{spec} .

The model developed and implemented here, describes the static and dynamic losses, for sake of simplicity, in one model. Additionally the z -axis represents the instantaneous specific losses p_{spec} [14].

3.2 Principle idea

The principle idea of the loss surface approach is, that when the instantaneous value of the flux density and the time derivative are known, the losses are clearly defined. So the losses are a function of $B(t)$ and $\frac{dB(t)}{dt}$

$$p_{\text{spec}} = f\left(B(t), \frac{dB(t)}{dt}\right). \quad (3.1)$$

So a surface is spanned in the $B(t)$ - $\frac{dB(t)}{dt}$ room, from which the name is derived Figure 3.1 shows such a surface for the material isovac 800-65 A

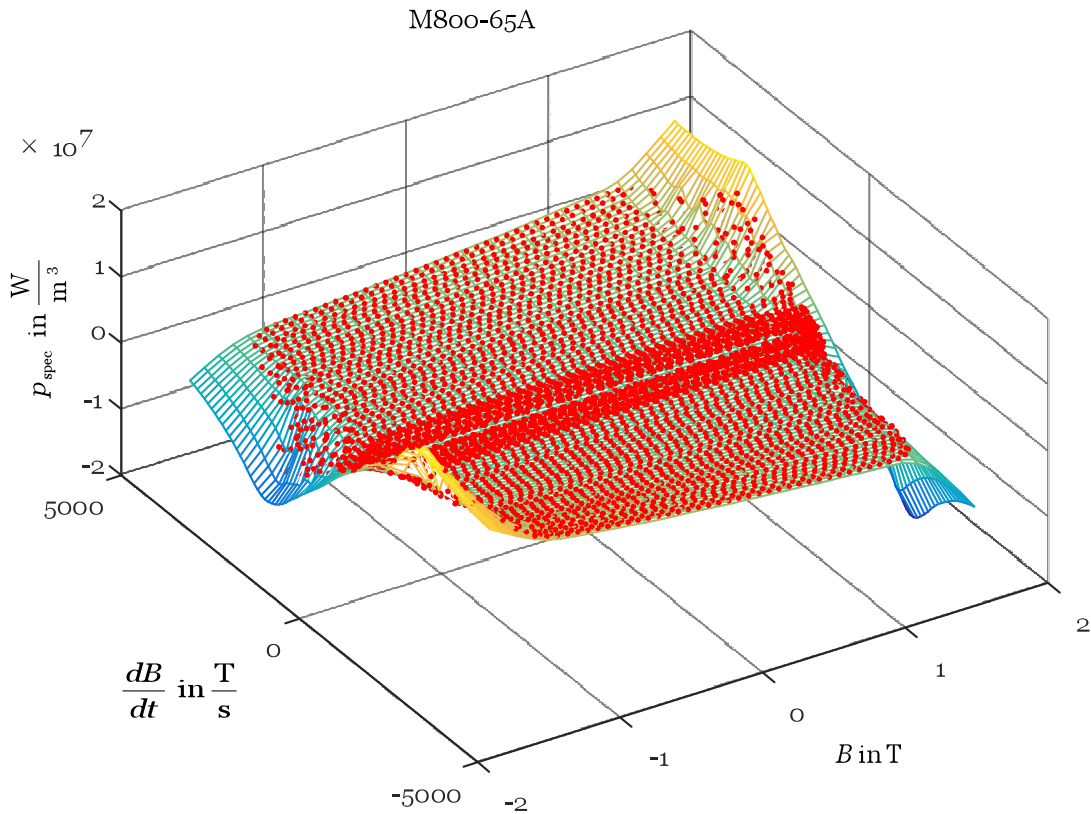


Figure 3.1: Loss surface for isovac 800-35A.

The red dots are supporting points derived from a measurement with an Epstein frame, the points for the mesh are calculated via a thin plate spline interpolation. With an arbitrary flux density waveform and the time derivative of it, it is possible, for every single time step, to determine the specific losses with help of the loss surface, so also the waveform of the iron loss power is known. With

$$P_{\text{mean}} = \frac{1}{T} \int_0^T p_{\text{spec}}(t) dt \quad (3.2)$$

the mean power per period can be calculated for the given flux density distribution.

3.3 Measurement waveform

The whole measurements were carried out, as far as possible, in agreement with the standard IEC 60404-2 „Magnetische Werkstoffe Teil 2: Verfahren zur Bestimmung der magnetischen Eigenschaften von Elektroblech und -band mit Hilfe eines Epsteinrahmens“ [31]. To present the surface in the $B(t)$ - $\frac{dB(t)}{dt}$ room, appropriate measurements have to be made. To support the surface well and interpolate between the points easier, the measurement points should be distributed as evenly as possible. With triangular flux density waveforms with different frequencies this could be achieved, because they have constant absolute values for $\frac{dB}{dt}$ for different values of B . These flux density waveforms lead to a shape of the secondary voltage of the Epstein frame which does not comply with the standard, but they allow deriving the loss surface from measurements. With sinusoidal voltages in the secondary winding, so also with sinusoidal flux densities, a large number of measurements have to be done, to support the loss surface well. Sinusoidal waveforms deliver supporting points located on an ellipse, because the flux density is sinusoidal and the time derivative is cosinusoidal with a different amplitude.

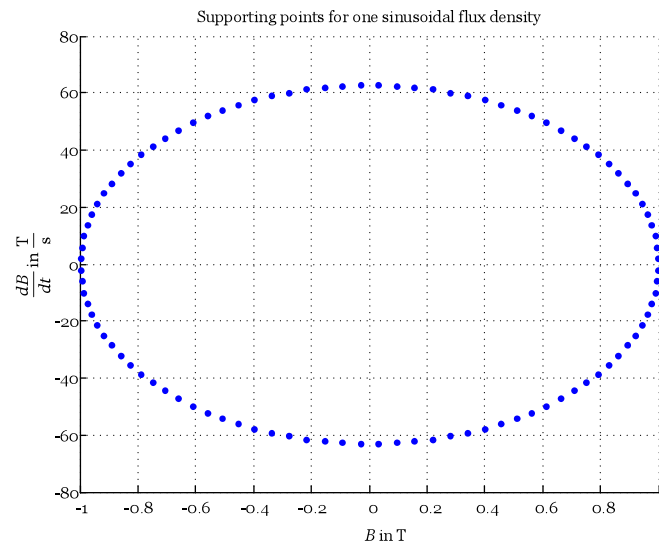


Figure 3.2: Supporting points for one sinusoidal flux density with $B = 1$ T and $f = 10$ Hz.

Figure 3.3 shows the supporting points for different measurements with sinusoidal flux densities. The amplitudes of the flux densities are 0.5 T, 1 T and 1.5 T, as can be seen on the vertexes of the ellipses. The frequencies are 10 Hz, 30 Hz and 50 Hz. For every amplitude all frequencies are measured. With increasing frequency the semi axes of the ellipses in the $\frac{dB}{dt}$ - direction extend, but the vertexes stay the same. It can be seen clearly that at some locations the measurement points are accumulating, whereas other regions are not supported, so a uniform distribution of the supporting points with a low number of measurements would be challenging. Another problem would be that some B - $\frac{dB}{dt}$ combinations would require curve parameters (u, f) that cannot be determined with the measurement setup.

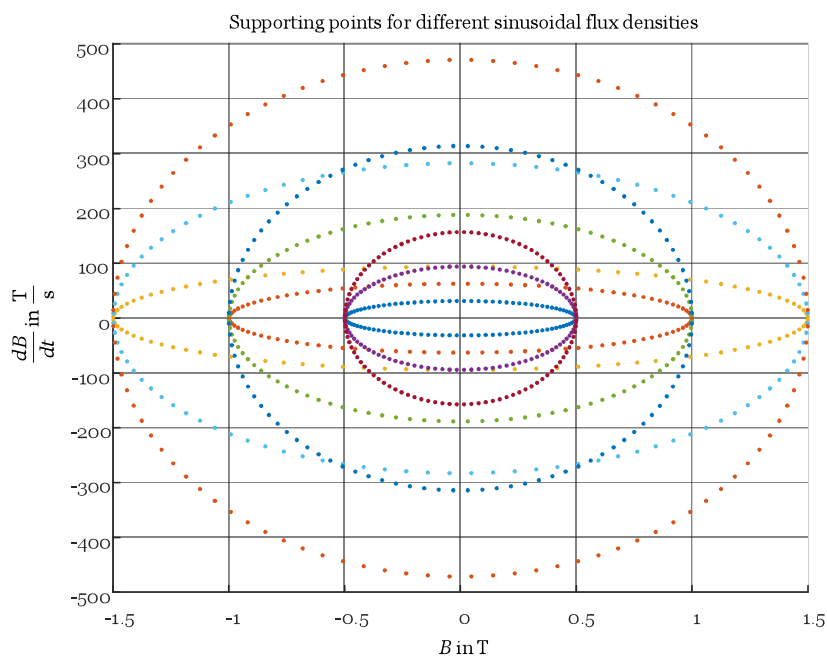


Figure 3.3: Supporting points for sinusoidal flux densities.

For these reasons, the supporting points were determined using a triangular flux density wave form. In the following picture the distribution of the measurement points for two triangular signals, with the same amplitude and different frequencies, in the B - $\frac{dB}{dt}$ plane are shown.

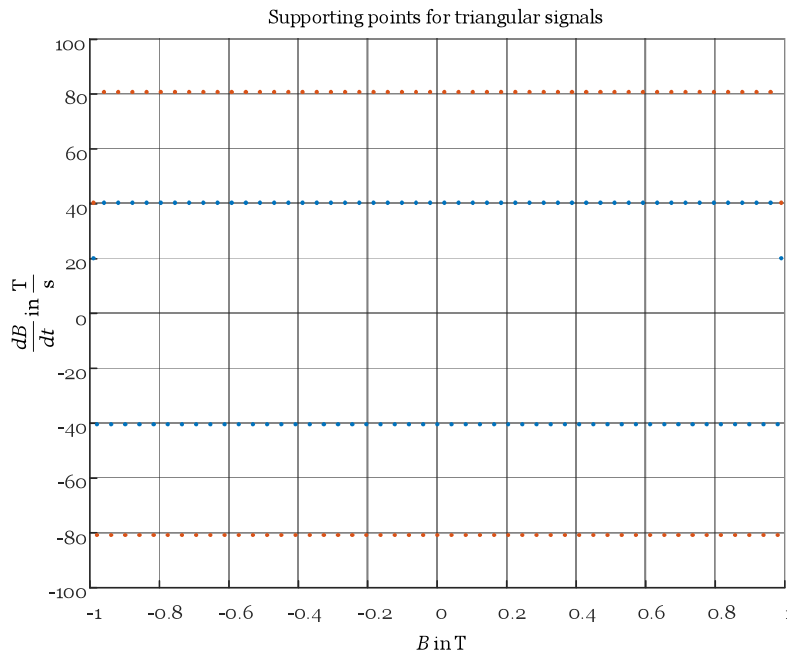


Figure 3.4: Supporting points for triangular flux densities.

Figure 3.5 shows a triangular flux density waveform with an amplitude A and the period T .

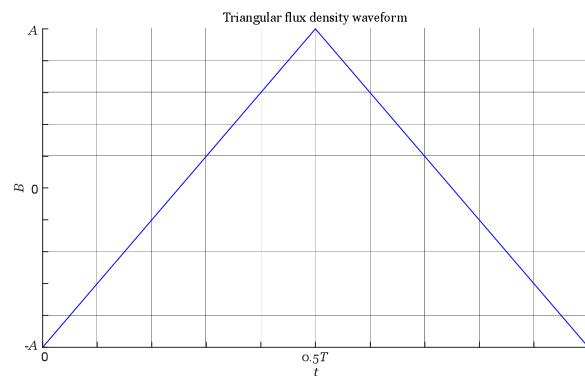


Figure 3.5: Triangular flux density waveform.

For triangular flux density waveforms

$$\frac{dB}{dt} = \frac{\Delta B}{\Delta t} \quad (3.3)$$

is valid. The time derivative for the ascending and the descending branch has the same absolute value. With $T = \frac{1}{f}$ and the amplitude of the flux density the

relationship of the time derivative gets

$$\left| \frac{dB}{dt} \right| = \frac{\Delta B}{\Delta t} = \frac{2A}{\frac{T}{2}} = \frac{4A}{\frac{1}{f}} = 4Af. \quad (3.4)$$

With (3.4) the frequency, for a desired value of $\frac{dB}{dt}$ and a fixed value for A , can be easily calculate. Because of

$$\Phi = \frac{1}{N} \int u(t)dt \quad (3.5)$$

and

$$B = \frac{\Phi}{A_{fe}} \quad (3.6)$$

a rectangular voltage has to be used to achieve a triangular flux density. In Figure 3.6 the voltage of the primary winding and the resulting flux density at a frequency of 300 Hz are shown.

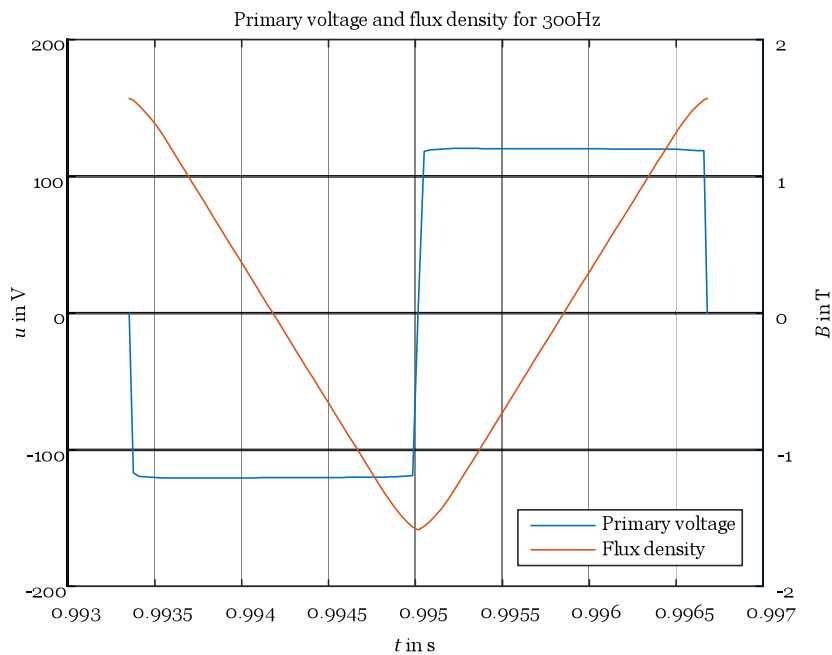


Figure 3.6: Primary voltage and flux density for 300 Hz.

3.4 Measurement setup

To obtain reproducible results attention was paid to built up a measurement setup in accordance with the standard IEC 60404-2 "Magnetische Werkstoffe Teil 2: Verfahren zur Bestimmung der magnetischen Eigenschaften von Elektroblech und -band mit Hilfe eines Epsteinrahmens" [31]. Because of the special characteristics of the loss surface approach, the measuring process and the evaluation of the measurement data differs slightly from the procedure in the standard

The main differences were:

- To determine the loss surface, a non sinusoidal waveform of the flux density was used, see Section 3.3.
- The readings were evaluated differently than in the standard, because instantaneous values were needed but the target of the standard are parameters of the waveform such as the effective or peak value. For example the iron losses, if they are calculated as in the standard, the result is the mean value of the iron losses for one period of the flux density waveform. But for the loss surface approach the instantaneous losses are needed.

In Figure 3.7 the block diagramm of the measurement setup is shown

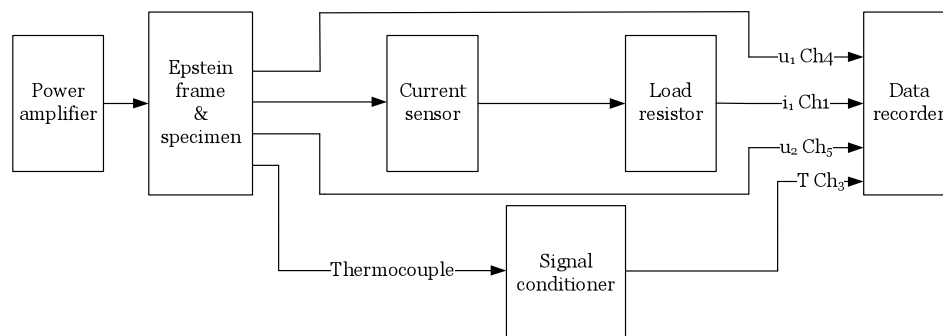


Figure 3.7: Block diagram of the measurement setup.

On the HBM data recorder a workbench was created, by loading this workbench all settings, like the filter setup, the usage of the different channels, some real time calculations and so on were set automatically. The following figure shows a photo of the measurement setup in the laboratory, the power amplifier cannot be seen in the picture.

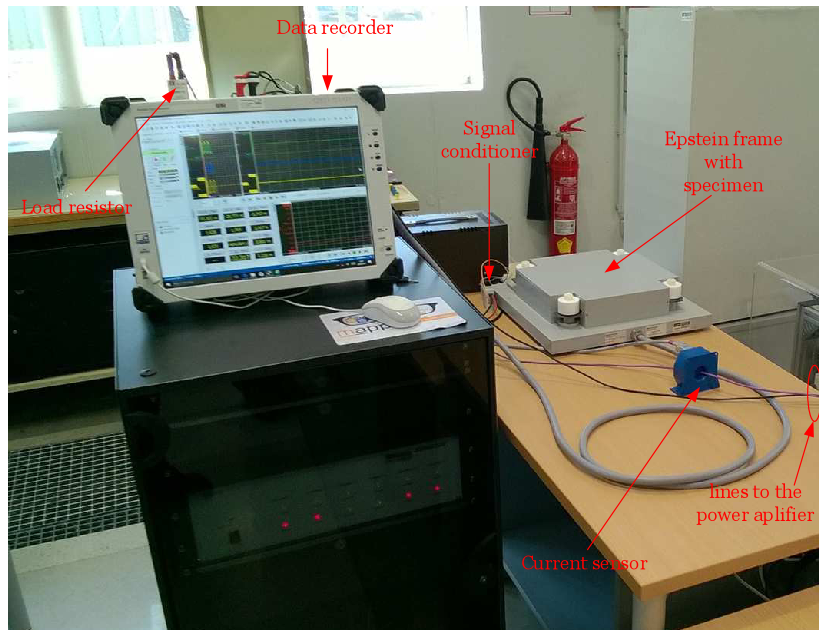


Figure 3.8: Used measurement setup.

3.4.1 Measurement equipment

In Table 3.1 an overview of the used devices is given.

3.4.2 Measurement process

To obtain the data every single measurement was carried out after a fixed procedure. Before the first measurement the specimen was demagnetized, to guarantee $J_0 = 0$.

- Set the frequency.
- Slowly increase the amplitude of the rectangular primary voltage till the current and so the magnetic field strength reach a previously defined value.
- Take the measurement and store the result.
- Slowly decrease the amplitude so that the specimen is demagnetized.
- With every measurement the iron losses heat up the specimen. If the next measurement could lead to a temperature which is not permissible, wait until the temperature has fallen far enough for the next measurement.

Scale	Sartorius Entris 6202 i-1s
Specimen	Voest alpine isovac 270-35A 32 pieces, $l = 305$ mm, $b = 30$ mm, $m = 0.77752$ kg
Epstein frame	Brockhaus measurements 700 windings primary and secondary
Power amplifier	Spitzenberger + Spies Three phase mains simulation system DM 1500/PAS
Current sensor	LEM IT 60-S Ultrastab
Load resistor	Steinbeis Transferzentrum Elas HBR10
Data recorder	HBM Portable data recorder Gen 3i
Signal conditioner	Status 1600T
Thermocouple	Typ K
Data evaluation	Personal computer
	MATLAB R2014b

Table 3.1: Used measurement devices.

3.4.3 Internal controller

The Epstein frame is a transformer in no load condition, so the voltage and the flux density are related with each other via (3.5) and (3.6). So it is desirable to control the secondary voltage of the Epstein frame. The used power amplifier provides a linear voltage controller to compensate the supply line voltage drop. For the feedback of the voltage, which should be controlled, a sense line is used. Initially, this controller was used to control the secondary voltage.

Sense line on the secondary side

In Figure 3.9 and Figure 3.10 the voltages and the current waveform for a frequency of 50 HZ are shown when the secondary voltage is controlled.

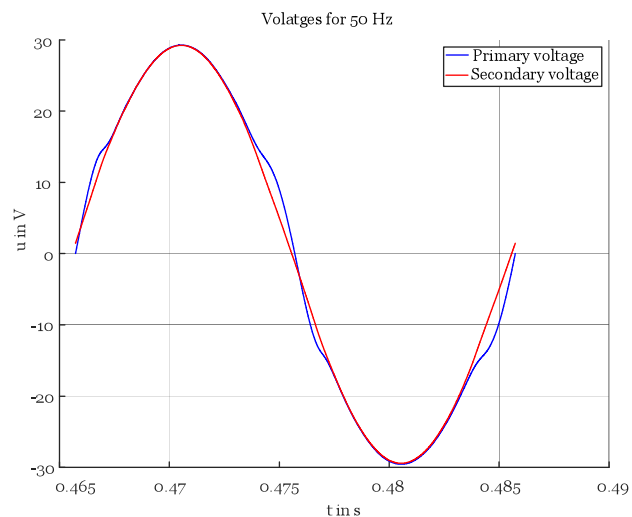


Figure 3.9: Primary and secondary voltage for 50 Hz with sense line on the secondary side.

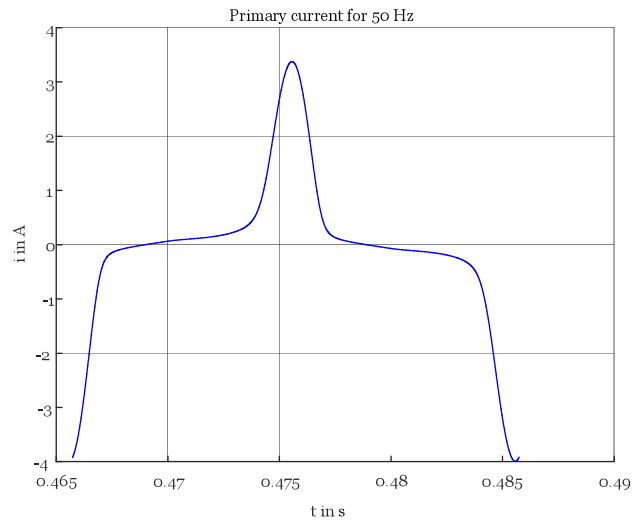


Figure 3.10: Primary current for 50 Hz with sense line on the secondary side.

Considering only the voltages the controller seems to work well, but the minimum and maximum peak value of the current differ about 0.5 A from each other. So this setup leads to a mean value in the current, although the coupling mode of the power amplifier was set to AC. This offset would alter the measurements. Figure 3.11 and Figure 3.12 show the measured waveforms when the internal controller is used to control the secondary voltage at a frequency of 500 Hz.

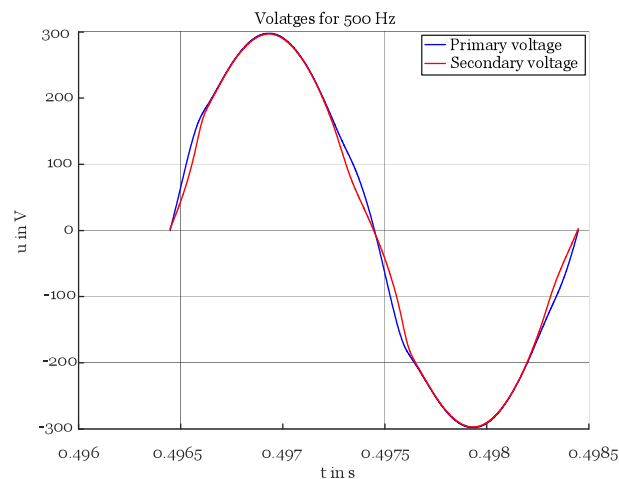


Figure 3.11: Primary and secondary voltage for 500 Hz with sense line on the secondary side.

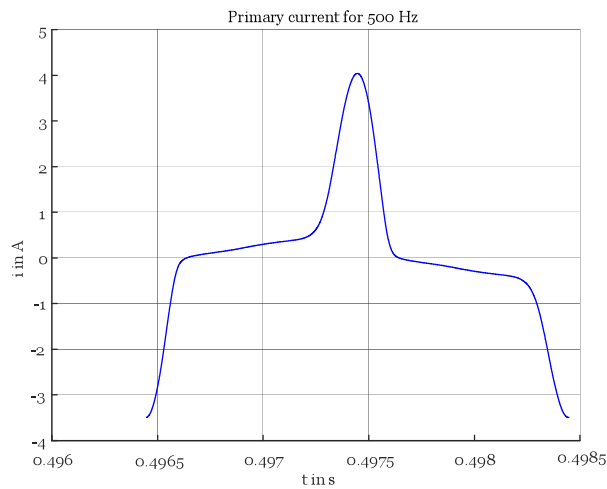


Figure 3.12: Primary current for 500 Hz with sense line on the secondary side.

Considering the voltages it seems that the controller is too slow to reach the desired waveform on the secondary side. Also the before mentioned offset in the current appears.

Sense line on the output of the power amplifier

Figure 3.13 and Figure 3.14 show the waveforms for 50 Hz, when the sense line is connected to the output of the power amplifier.

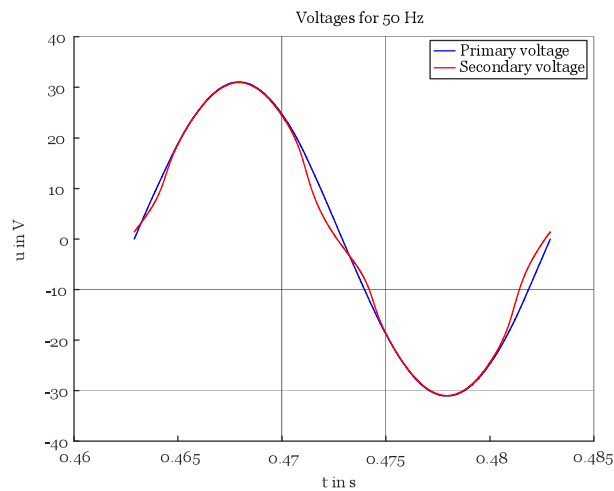


Figure 3.13: Primary and secondary voltage for 50 Hz with sense line on the output of the power amplifier.

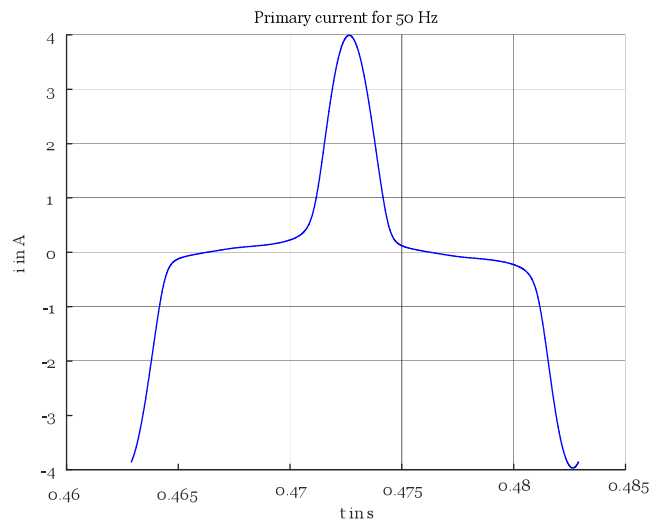


Figure 3.14: Primary current for 50 Hz with sense line on the output of the power amplifier.

The offset in the current is gone but the secondary voltage has not the desired waveform any more.

Figure 3.15 and Figure 3.16 show the waveforms for a frequency of 500 Hz with the sense line connected to the output of the power amplifier.

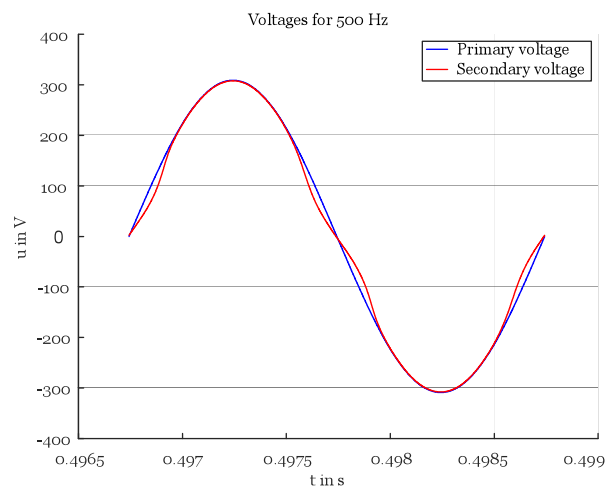


Figure 3.15: Primary and secondary voltage for 500 Hz with sense line on the output of the power amplifier.

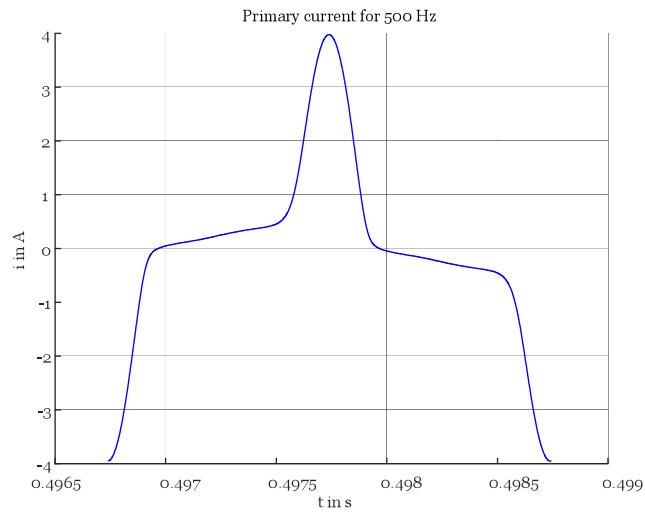


Figure 3.16: Primary current for 500 Hz with sense line on the output of the power amplifier.

The primary voltage is sinusoidal again and the offset in the current is gone.

Conclusion

Summarizing the results of these measurements, the internal controller should not be used to control the secondary voltage, because of the appearing offset in the current and it seems that it is too slow to work well at higher frequencies. In addition a request has revealed that the use of the internal voltage controller on the secondary side of the Epstein frame is prohibited by the manufacturer. Therefore, for further measurements the sense line was always connected to the output of the power amplifier.

3.5 Calculations

The measurement setup shown in Section 3.4 does not allow measuring the magnetic field strength and the flux density directly, so they have to be derived from the measured quantities. With Ampere's law, the magnetic path length and the number of primary windings of the Epstein frame, the magnetic field strength H is calculated

$$H = \frac{N_1 i}{l}. \quad (3.7)$$

The Epstein frame represents a transformer in the no load condition with compensated air flux. That means if no specimens are in the Epstein frame, the voltage in the secondary winding is zero. So with an Epstein frame the magnetic polarisation is measured. The polarisation and the voltage in the secondary winding are linked via (3.8)

$$J = \frac{1}{N_2 A_{fe}} \int u_2 dt + J_0. \quad (3.8)$$

Because the specimen is demagnetized before the measurement $J_0 = 0$. The cross section of the iron A_{fe} can be calculated with (3.9) [31]

$$A_{fe} = \frac{m}{4\rho l}. \quad (3.9)$$

In electric drives the quantity of interest is the magnetic flux density and not the polarisation and so the air flux also has to be taken into account

$$B = \mu_0 H + J. \quad (3.10)$$

With the flux density over the time it is possible to determine the time derivative $\frac{dB}{dt}$ and with the field strength H the specific losses [14].

$$p_{\text{spec}} = H \frac{dB}{dt}. \quad (3.11)$$

The quantities B , $\frac{dB}{dt}$ and p_{spec} are the coordinates for the supporting points of the loss surface. With these points and a suitable interpolation method the losses for any arbitrary flux density waveform can be calculated.

All measurements were taken with a sample rate of $2 \frac{Ms}{s}$. The measurement noise was eliminated by a moving mean filter. The highest measured frequency was 600 Hz, with the used sample rate this gives about 3333 samples per period, so that means that every measured frequency would give $\frac{2 \cdot 10^6}{f} \frac{s}{\text{period}}$. When the number of supporting points for the loss surface increases, also the computational time and the demand for storage rises, so the number of supporting points per frequency was limited. The filtered and downsampled data were used to generate the supporting points of the loss surface.

3.6 Evaluation of the measurement results

As mentioned before, the Epstein frame is a transformer in no load condition, so the secondary current is zero and therefore the voltage at the secondary winding is equal to the voltage at the inductivity L_h .

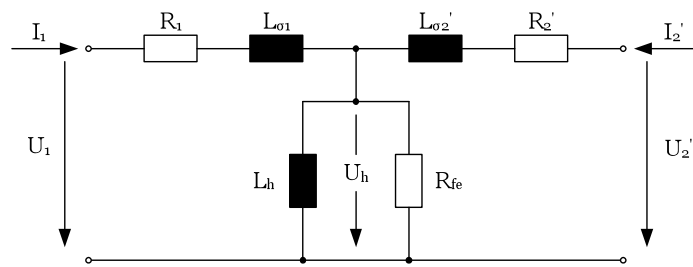


Figure 3.17: Equivalent circuit of the Epstein frame.

So the equivalent circuit diagram simplifies to:

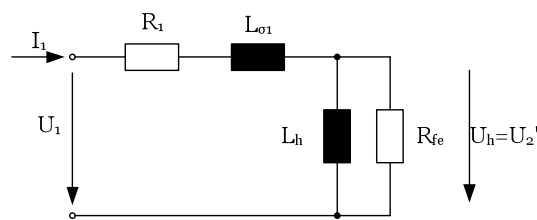


Figure 3.18: Simplified equivalent circuit of the Epstein frame.

For nonsinusoidal waveforms the power can be calculated as follows

$$P_{\text{mean}} = \frac{1}{T} \int_{t=t_1}^{t_1+T} i(t)u(t)dt. \quad (3.12)$$

The specific iron losses are derived from the secondary voltage, the primary current and the magnetic active volume

$$p_{\text{fe, mean}} = \frac{1}{Tl_m A} \int_{t=t_1}^{t_1+T} i_1(t)u_2(t)dt. \quad (3.13)$$

$p_{\text{fe, mean}}$...	specific iron losses in $\frac{\text{W}}{\text{m}^3}$
l_m	...	magnetic path length $l_m = 0.94\text{m}$
A	...	cross section of the specimen in m^2

With (3.13) the iron losses in the magnetic active volume are calculated from measured values and hence it can be used as a tool to verify the results of the two introduced iron loss models.

3.6.1 Measurement accuracy

The measured iron losses, which are the supporting points for the loss surface, are not measured directly, they are derived from several measured quantities. Each measurement is subject to a certain error and contributes to the total error. The Epstein frame has a compensation winding, so not the flux density B , but the polarisation J is measured. Equation (3.10) shows the connection between the flux density and the polarisation. The maximum contribution of the $\mu_0 H$ - term to the flux density is in the range of a few mT, but would lead to a second order time derivative of the current in the formula for the complete error. The approximation of the second order time derivative via the difference quotient could lead to results, which are not reliable any more, as it is the case here. For future measurements ring shaped specimen without a compensation winding will be used and so the flux density is measured,

see Section 5.2. So for sake of simplicity the $\mu_0 H$ - term in (3.10) is neglected, so (3.8) becomes

$$B = \frac{1}{N_2 A_{fe}} \int u_2 dt + B_0. \quad (3.14)$$

Again B_0 is, due to the demagnetization, zero. (3.11) shows that the iron losses are a function of the time derivative of the flux density $\frac{dB}{dt}$ and the field strength H . (3.14) rewritten gives the time derivative of the flux density

$$\frac{dB}{dt} = \frac{u_2}{N_2 A_{fe}}. \quad (3.15)$$

With (3.7), $N_1 = N_2$ and (3.9) the instantaneous iron losses can be written as

$$p = H \frac{dB}{dt} = \frac{4\rho}{l_m} \frac{u_2 l i}{m}. \quad (3.16)$$

- ρ ... density of the material
- l_m ... effective magnetic path length
- u_2 ... voltage in the secondary winding of the Epstein frame
- l ... length of the iron strips
- i ... current in the primary winding
- m ... total mass of the iron

The density of the material ρ is given by the manufacturer in the data sheet and the magnetic length l_m is given in the standard IEC 60404-2 „Magnetische Werkstoffe Teil 2: Verfahren zur Bestimmung der magnetischen Eigenschaften von Elektroblech und -band mit Hilfe eines Epsteinrahmens“ [31], so these two quantities are assumed as constant, without any influence on the measurement error. To calculate the worst case error the following formula can be used

$$\Delta y(x_1, \dots, x_n) = \sum_{i=1}^n \left| \frac{\partial y}{\partial x_i} \right| \Delta x_i. \quad (3.17)$$

- Δy ... total error of the calculated size y
- x_1, \dots, x_n ... measurement sizes from which y is derived
- Δx_i ... error of the single measurement sizes

The sizes u_2 , i , l and m have influence on the measurement error, so Δp becomes

$$\Delta p = \frac{4\rho}{l_m} \left(\left| \frac{li}{m} \right| \Delta u_2 + \left| \frac{u_2 l}{m} \right| \Delta i + \left| \frac{u_2 i}{m} \right| \Delta l + \left| \frac{u_2 li}{m^2} \right| \Delta m \right). \quad (3.18)$$

With (3.18) it is possible to estimate the maximal error, when all single errors occur with their full strength and in such a way that they all act in one direction. The occurrence of such a scenario is unlikely, so in general the measurement error can be assumed smaller than the maximal possible error Δp . To give the calculated maximum measurement error a meaning, it is related to the maximum absolute value of the iron loss power for each measurement. So for all values from the measurement at 50 Hz the reference value is the maximum absolute value of the iron loss power at this frequency

$$e = 100 \cdot \frac{\Delta p}{p_{\max, \text{abs}}(f_{\text{meas}})}. \quad (3.19)$$

e	...	error in %
Δp	...	total error for one measurement point
$p_{\max, \text{abs}}(f_{\text{meas}})$...	maximum absolute value of the measured power at the considered frequency

With a maximum for the error with about 3% and a mean value of 1.5% the measurement setup is supposed to be reliable. Of course these values are only for one certain measurement, for an other measurement the values of the errors will change, but they should be in the same range.

3.7 Interpolation

It is impossible to record all B - $\frac{dB}{dt}$ combinations, which could occur in the region of interest, so a suitable method for interpolation has to be found. For this reason two techniques from the family of distance based interpolation methods were considered, the inverse distance weighted interpolation (IDWI) and the thin plate spline interpolation (TPSI). In the family of these interpolation methods all, or only a certain number of measurement points, influence the result. The influence of a

specific measurement point on the interpolation depends on its distance to the point of interest.

3.7.1 Inverse distance weighted interpolation - IDWI

For the inverse distance weighted interpolation the value at any point is given with [32]

$$\hat{z}(x_o) = \sum_{i=1}^k \lambda_i z(x_i) \quad (3.20)$$

where the coefficient λ_i is given with

$$\lambda_i = \frac{\frac{1}{d_{i_o}^p}}{\sum_{i=1}^k \frac{1}{d_{i_o}^p}}. \quad (3.21)$$

- $\hat{z}(x_o)$... value at the point of interest x_o
- k ... number of considered points
- $z(x_i)$... value at the measurement point x_i
- p ... exponent to control the influence of the single points
- d_{i_o} ... distance between point x_o and the point x_i

The exponent p controls the influence of the single points on the result. The lower p the more uniformly every single point contributes to the result. With increasing p the influence of points, that are far way from the point of interest, is decreasing. It is also possible to restrict the number of points which have influence on the result, for this there are two possibilities:

- Fixed radius: A fixed radius is defined and all points within this radius influence the calculation.
- Fixed number of points: The number of points which influence the result is defined, so only the k nearest points are considered.

With the second method, $k = 4$ and $p = 0.1$ the following surface is obtained:

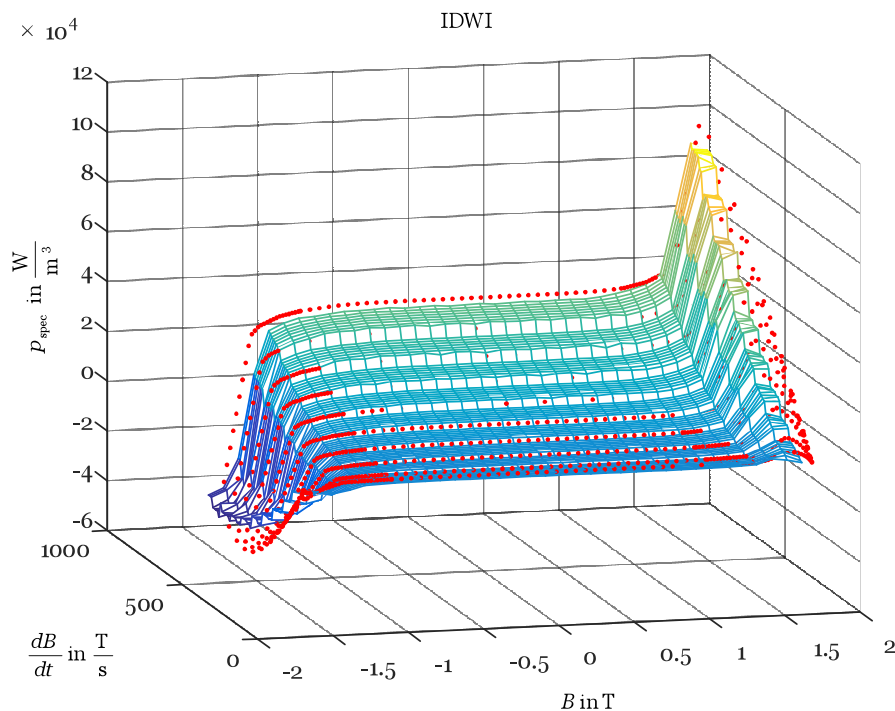


Figure 3.19: Surface for the IDWI with $n = 4$ and $p = 0.1$.

The data for this surface are from a Simulink model of a transformer with a saturable core. The parameters p and n were chosen deliberately poorly to show the problems which could occur with the IDWI and for a better view only half of the positive derivatives of the flux densities are presented. The inverse distance weighted interpolation is a method where the surface is not forced to fit the measured points and it also has no smooth shape. It is clear that with a more suitable set of parameters these effects could be reduced, but they would never disappear completely and the parameters have to be determined iteratively. An additional effect, not visible in Figure 3.19 but likely to appear, are the so called bull eyes. These are circular artefacts, which have the same value, around the measurement points. To avoid the problems of the IDWI the thin plate spline interpolation was considered subsequently.

3.7.2 Thin plate spline interpolation - TPSI

The thin plate spline interpolation is an interpolation method based on a radial basis function, this is a function which only depends on the distance of the origin. The

thin plate spline is described as follows

$$y(r) = r^2 \ln(r). \quad (3.22)$$

This curve shape describes the position of a thin metal sheet or rubber membrane. So it is tried to find a surface which goes exactly through the given points and takes the state of the lowest energy in between, thus bending as little as possible in the intermediate spaces. Bending as little as possible means that the bending energy is minimized. For the interpolation a thin plate spline is placed on every measurement point and with the weighted sum of all these splines, the values of the surface at an arbitrary position can be determined. Described in a mathematical way [33]

$$s(\underline{x}_i) = f_i \quad i = 1, 2, \dots, n \quad (3.23)$$

$$V(s) = \int_{\mathbb{R}^2} \left(\frac{\partial^2 s(\underline{x})}{\partial x^2} \right)^2 + 2 \left(\frac{\partial^2 s(\underline{x})}{\partial x \partial y} \right)^2 + \left(\frac{\partial^2 s(\underline{x})}{\partial y^2} \right)^2 d\underline{x}. \quad (3.24)$$

- $s(\underline{x}_i)$... value of the surface at the point \underline{x}_i
- n ... number of measurement points
- f_i ... given supporting point
- $V(s)$... bending energy, which should be minimized
- x and y ... components of \underline{x}

The surface which fulfils these requirements is given with the thin plate spline via (3.25)

$$s(\underline{x}) = \sum_{i=1}^n \lambda_i \|\underline{x} - \underline{x}_i\|^2 \ln \|\underline{x} - \underline{x}_i\| + c_0 + c_1 x + c_2 y \quad \underline{x} \in \mathbb{R}^2. \quad (3.25)$$

- \underline{x} ... point of interest
- λ_i ... weighting factor for every single thin plate spline
- $\|\underline{a}\|$... Euclidean norm of \underline{a}
- c_0, c_1 and c_2 ... global parameters

Thereby the coefficients λ have to meet the following

$$\sum_{i=1}^n \lambda_i = \sum_{i=1}^n \lambda_i x_i = \sum_{i=1}^n \lambda_i y_i = 0. \quad (3.26)$$

The above mentioned requirements can be rewritten in the following system of equations

$$\begin{pmatrix} \Phi & P \\ P^T & 0 \end{pmatrix} \begin{pmatrix} \underline{\lambda} \\ \underline{c} \end{pmatrix} = \begin{pmatrix} \underline{f} \\ 0 \end{pmatrix}. \quad (3.27)$$

- Φ ... $n \times n$; with the elements $\left\| \underline{x}_i - \underline{x}_j \right\|^2 \ln \left\| \underline{x}_i - \underline{x}_j \right\| : i, j = 1, 2, \dots, n$
 P ... $n \times 3$; with the rows $(1 \ x_i \ y_i)$
 $\underline{\lambda}$... $n \times 1$; vector with the weighting factors
 \underline{c} ... 3×1 ; c_0, c_1 and c_2
 \underline{f} ... $n \times 1$; supporting points from the measurement

The matrix of this equation system is nonsingular, therefore with a unique solution and so with a unique surface. Solve the equation system for $\underline{\lambda}$ and \underline{c} and subsequently evaluate (3.25) on the desired positions the following surface is obtained for the material isovac 270-35A and a specimen width of 30 mm, again the red dots are the supporting points and the mesh is the interpolated surface.

It can be seen that the surface coincides with the measurement points, according to 3.23 and the distinctive discontinuities, which could occur with the IDWI (see Figure 3.19), are gone. An other big advantage is that no parameters have to be tuned manually.

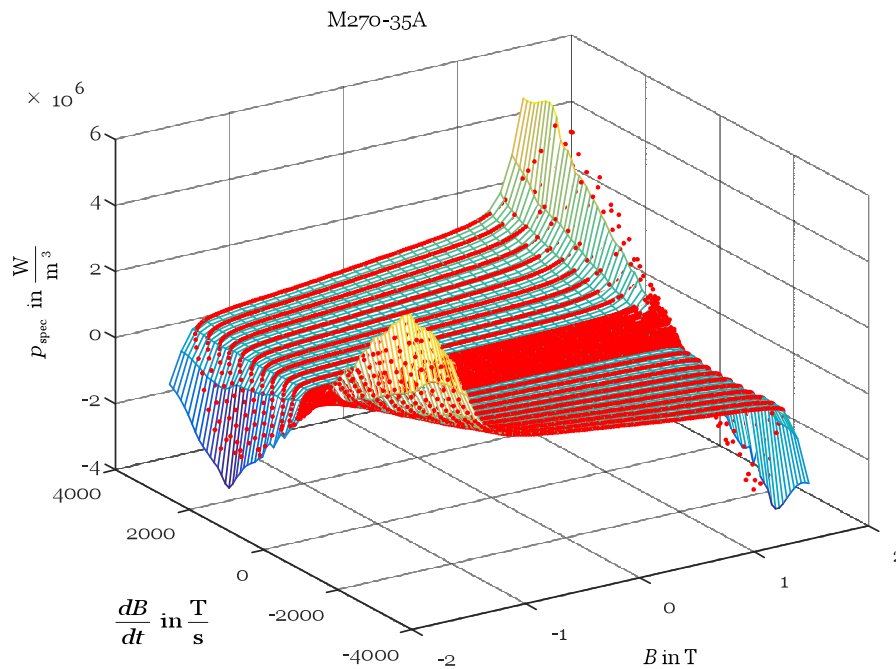


Figure 3.20: TPSI surface for isovac 270-35A.

3.8 Considerations regarding the Epstein frame

The magnetic ideal specimen would be a toroidal core with a constant cross section and constant magnetic properties along the circumference. These specimens have to be wound by hand and so it takes some time to prepare them for the measurements. In the industry the wish for a faster procedure lead to the Epstein measurements, in 1940 the 25cm Epstein frame was introduced. The currently applicable standard for these measurements is IEC 60404-2 „Magnetische Werkstoffe Teil 2: Verfahren zur Bestimmung der magnetischen Eigenschaften von Elektroblech und -band mit Hilfe eines Epsteinrahmens“ [31], here the measurement setup and process are described. This setup has a few drawbacks that could affect the results depending on the flux density range, in which the measurements are taken [34].

- The cross section is not uniform.
- There are sharp edges for the flux in the corners, so the flux distribution is not uniform.

- Due to the nonuniformities of the cross section and the flux distribution the magnetic path length is set to 0.94 m.
- The preparation of the Epstein set influences the magnetic properties of the material. Depending on the used procedure to prepare the Epstein set, e.g. punching or laser cutting, the material properties on the edges are deteriorated, so higher losses occur. [35] This influence is very distinctive when grain oriented steel is used. So if grain oriented steel is used, the Epstein set has to be annealed before measurements are taken, to reduce this influence at least partially. If there was any internal stress in the original sheet, it cannot be detected, due to the annealing. [36]

Despite these drawbacks, the Epstein frame is still a very often used approach to determine the magnetic behaviour of electric steel. In the following figure the basic structure of an Epstein frame is shown [20].

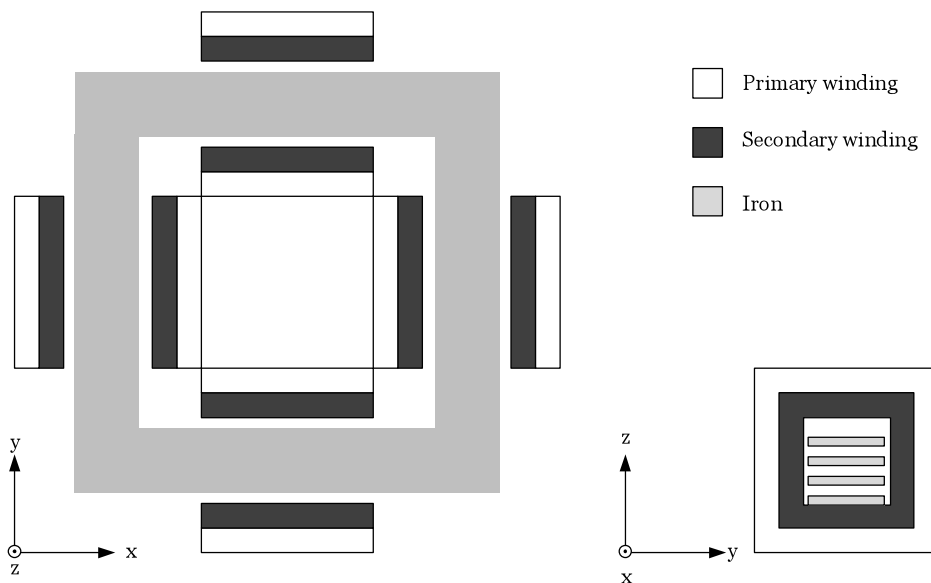


Figure 3.21: Basic structure of an Epstein frame [20].

The iron is stacked as it is shown in Figure 3.22. The primary winding and the secondary winding surround the stripes at every leg, where the secondary winding, which is the measurement winding, is the inner one. The primary winding is needed to build up the magnetic field, to which the iron is exposed and is located in the outer layer.

3.8.1 Effective magnetic path length

Due to the evaluation of the measurements with the agreed path length of 0.94 m, a systematic error is made. For the 25cm Epstein frame the magnetic path length was set to 0.94 m under the following consideration [34].

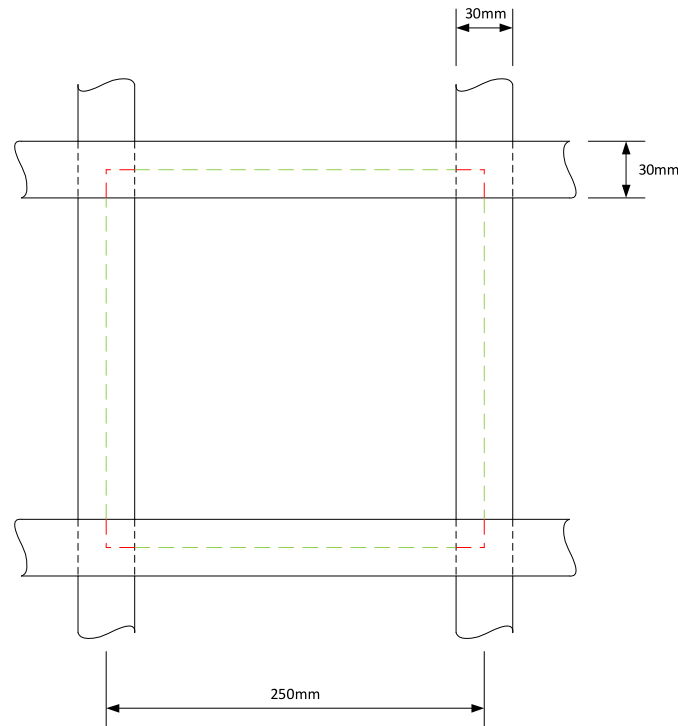


Figure 3.22: Magnetic path length of the Epstein frame.

The stripes are stacked in the Epstein frame in such a way, that they overlap in the corners, so the cross section in the corners is twice as large as in the legs. With the assumption, that the specimen has linear behaviour, the path in the edges is weighted with the factor 0.5, resulting in

$$l_m = 4 \cdot (250\text{mm} - 30\text{mm}) + 4 \cdot \frac{30\text{mm}}{2} = 0.94\text{m}. \quad (3.28)$$

When the flux density increases and so the material behaviour becomes non linear, the assumption with the weighting factor for the corners is not valid any longer. A simple approach to correct the effective magnetic path length as a function of the

state of the material is shown in [37]

$$l_{m\mu} = l_l + \frac{\mu_l}{2\mu_c} l_c \quad (3.29)$$

where $\mu_l = \mu(\hat{j})$ and $\mu_c = \mu(\frac{j}{2})$.

$l_{m\mu}$... effective magnetic path length

l_l ... magnetic path length in the legs

l_c ... magnetic path length in the corners

μ_l, μ_c ... permeability of the legs respectively of the corners

So for the 25 cm- Epstein frame

$$l_{m\mu} = 880 \text{ mm} + \frac{\mu_l}{\mu_c} 60 \text{ mm}. \quad (3.30)$$

These constraints and the demand for a faster procedure lead to the single sheet tester, which is often used by the manufacturers of electric steel nowadays. Due to the fact that the single sheet tester is a big and heavy device and there is a great treasure of experience for the Epstein frame, the Epstein frame is still used in many laboratories. A comparison of the two testing systems is given in [37].

3.9 Conclusion

The loss surface approach is a measurement based approach, so it is a bit more complex to obtain the needed data for it compared to the iGSE. This disadvantage is compensated by the fact that influences like the cutting process can be taken into account. The used measurement setup contains an Epstein frame, which leads to some disadvantages, as shown in Section 3.8, to overcome these, ring shaped specimen should be used in future. Although an Epstein frame is used and no controller was implemented to control the shape of the flux density, the results are very satisfying, see Table 4.2. The discrepancies at low $\frac{dB}{dt}$, as can be seen in Figure 4.5, should become smaller when the before mentioned controller is used. So the loss surface approach can be regarded as good tool for the iron loss estimation with any flux density waveform. Some additional work should allow solving the mentioned problems with the loss surface approach.

Chapter 4

Comparison of the iGSE and the loss surface approach

4.1 Introduction

In this chapter the two described iron loss models are compared to each other. For this reason measurements were made with the Epstein frame, three different waveforms and specimens of the material isovac 270-35 A. The iron losses were calculated via (3.13) and served as reference for the comparison with the modelled iron losses.

4.2 Waveforms

With the used measurement setup it was only possible to specify the primary voltage and so indirectly the flux density in the specimen. The following table shows the harmonics and the phase angles of the single harmonics for the three used voltage waveforms, which were applied on the primary side of the Epstein frame.

Waveform	Harmonics	Amplitude	Phase
-	-	%	°
1	1	100	0
2	1	100	0
	3	50	0
	5	10	180
3	1	100	0
	3	30	180

Table 4.1: Primary voltage forms.

All voltage forms were measured at 50 Hz, 150 Hz, 250 Hz and 500 Hz frequency. The amplitude of the signal was chosen in a way, that the maximum of the current was approximately 2 A and so the maximum of the flux density was about 1.5 T. Figure 4.1 shows exemplarily the composition of voltage waveform 2 in Table 4.1. Figures 4.2 to 4.4 show the measured primary voltage and the calculated flux density, all for a frequency of 150 Hz.

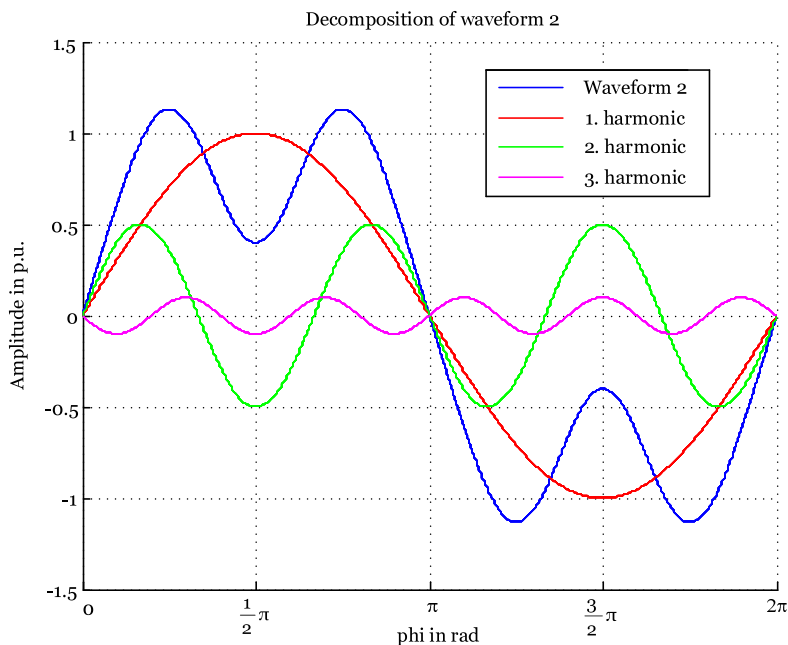


Figure 4.1: Decomposition of waveform 2 of Table 4.1.

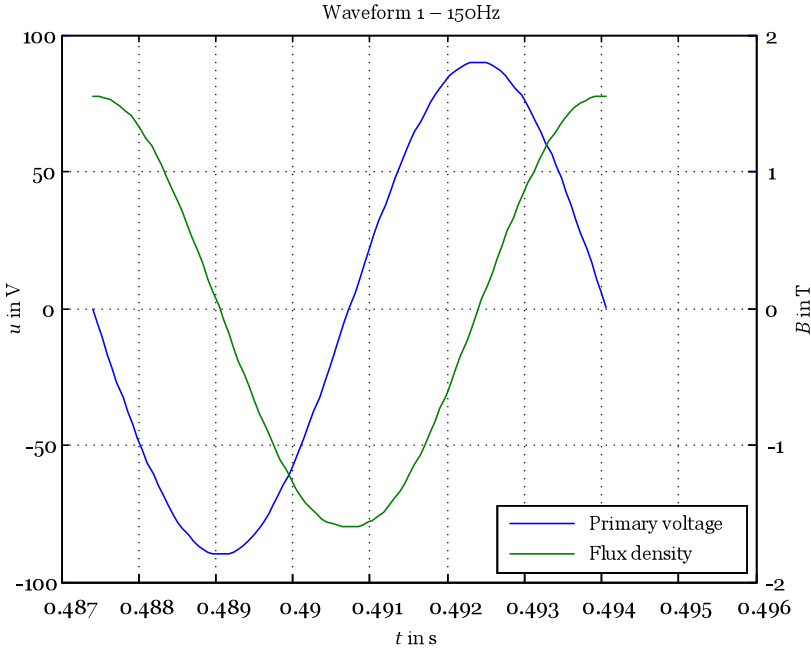


Figure 4.2: First waveform of Table 4.1.

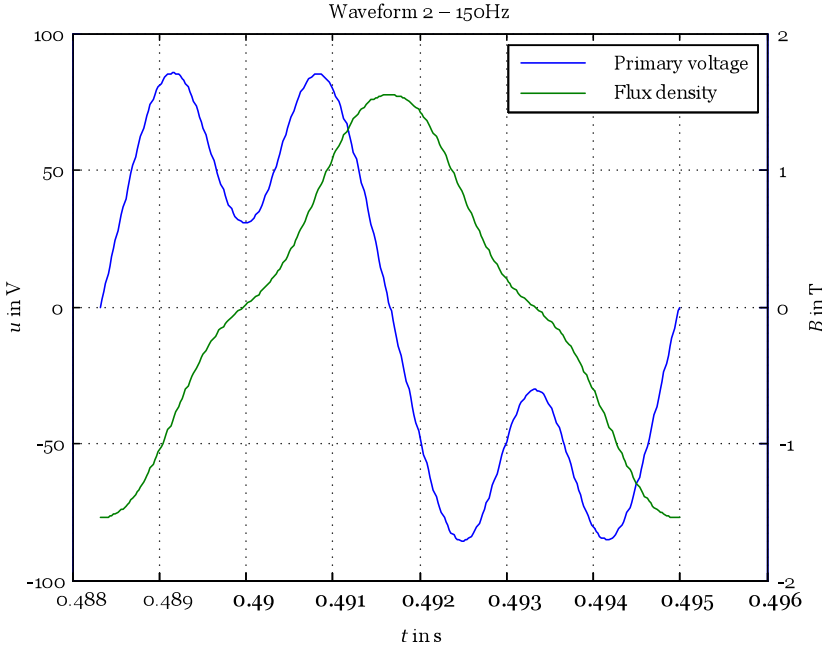


Figure 4.3: Second waveform of Table 4.1.

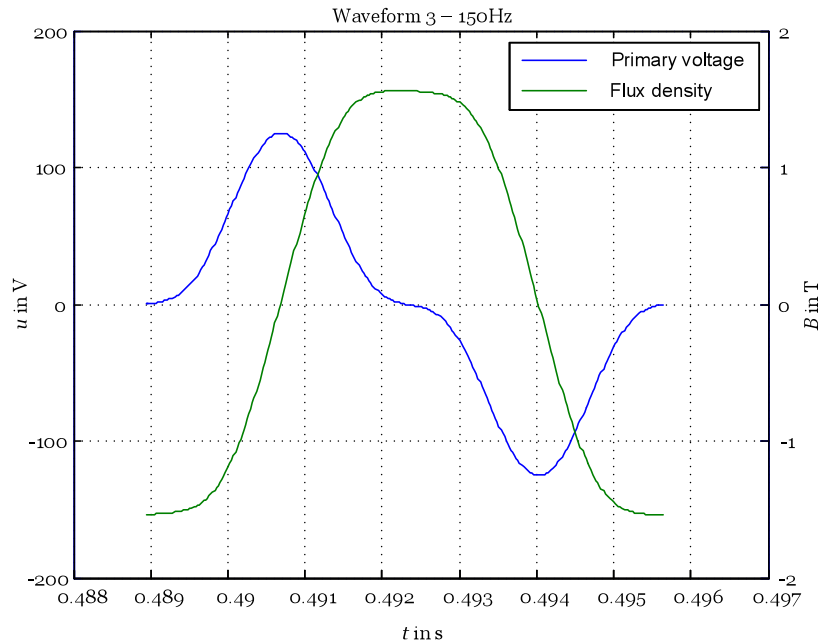


Figure 4.4: Third waveform of Table 4.1.

4.3 Results

The following table shows the results of the measurements and the calculated iron losses. As mentioned before the measured iron losses served as reference for the comparison. The error is calculated as follows

$$error = 100 \cdot \frac{p_{fe, calc} - p_{fe, meas}}{p_{fe, meas}}. \quad (4.1)$$

4.3.1 Results of the iGSE

To be able to use the iGSE, the Steinmetz parameters of the material have to be known. They were estimated for the used material as shown in Section 2.5 from the data provided of the manufacturer [38].

The iGSE does not calculate the instantaneous losses such as the loss surface approach, it only gives the total iron losses for one period of a certain flux density

Waveform	f	$p_{fe, meas}$	$p_{fe, iGSE}$	$error$	$p_{fe, LS}$	$error$
-	Hz	$\frac{W}{m^3}$	$\frac{W}{m^3}$	%	$\frac{W}{m^3}$	%
1	50	21893	21492	-1.8	21934	0.2
	150	90263	93178	3.2	87774	-2.8
	250	186414	190622	2.3	185390	-0.6
	500	533573	591931	10.9	534086	0.1
2	50	20938	20176	-3.6	20404	-2.6
	150	83778	86714	3.5	85694	2.3
	250	174873	177727	1.6	177852	1.7
	500	501873	554132	10.4	515575	2.7
3	50	22319	22107	-1	21895	-1.9
	150	95128	98653	3.7	96412	1.3
	250	203800	202257	-0.8	205427	0.8
	500	520897	513432	-1.4	526429	1.1

Table 4.2: Comparison of the results.

waveform. So it is not possible to compare the measured iron loss curve with a calculated one, but it seems that the error is smaller for signals where the flux density has regions with a low $\frac{dB}{dt}$, where the $\left|\frac{dB}{dt}\right|^\alpha$ term in (2.1) is smaller. Another reason for the difference in the measurement results could be that the manufacturer of the used iron uses a single sheet tester to gain the data for the data sheet and the measurements were carried out with an Epstein frame. According to [37] the results of the Epstein frame and the single sheet tester differ, especially for higher flux densities. Nevertheless the results agree within an acceptable range.

4.3.2 Results of the loss surface approach

In Figure 4.5 $\frac{dB}{dt}$ and B , each normalized on their maximum value, such as the measured iron losses and the via the loss surface approach calculated losses, both normalized on the measured iron losses, are shown. As can be seen, the two loss curves fit very well, the biggest discrepancies occur for high values of B and low $\frac{dB}{dt}$. These points are located in the area of the loss surface, where one part raises very quickly in the positive direction and one part falls very rapidly in the negative

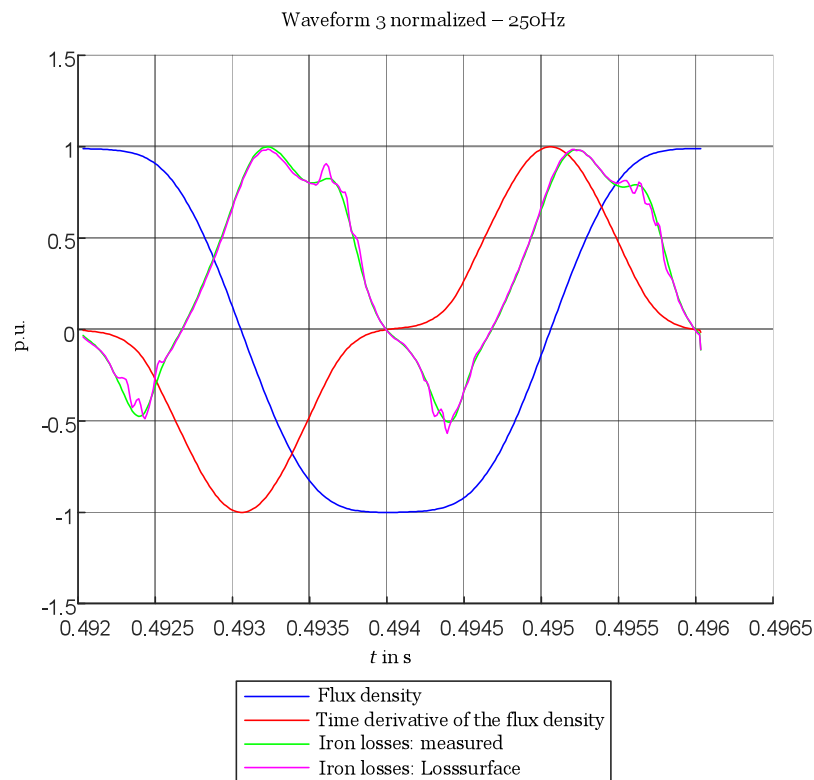


Figure 4.5: Normalized curve shapes of the third waveform.

one, such as it can be seen in Figure 3.1 or in Figure 3.20. For supporting points at low $\frac{dB}{dt}$ values, measurements with low frequencies are needed. As shown in Figure 5.1 the shapes of the waveforms for low frequencies do not match with the desired measurement waveforms, because no controller was implemented. The used waveforms at low frequencies have a flat top, so a nearly constant B and a $\frac{dB}{dt}$ which is very small. So measurement points, which should be distributed evenly over the B - $\frac{dB}{dt}$ plane, accumulate in the before mentioned area of the surface, where one part raises very quickly in the positive direction and one part falls very rapidly in the negative one. The used radial basis function interpolation forces the surface to go through the measured supporting points, so the surface looks in these regions a bit wrinkled. This is also reflected in the calculated iron losses when the parameters of the considered flux density are in these regions, a small change in the coordinates results in a big change in the iron losses and so the above mentioned discrepancies occur. So it is recommended to design a controller, to control the shape of the flux density waveforms, take the measurements for the loss surface and compute the iron

losses again.

Figure 4.6 shows the resulting curve shapes for the third waveform and a frequency of 500 Hz. Table 4.2 shows an error of only 1.1 % but considering Figure 4.6 more closely shows that the predicted and measured losses do not match very accurately for high absolute values of $\frac{dB}{dt}$. The reason why the error is very small, is that for positive values of $\frac{dB}{dt}$ the predicted iron losses are higher than the measured losses and for negative values of $\frac{dB}{dt}$ the losses are lower, so in average the error is very small.

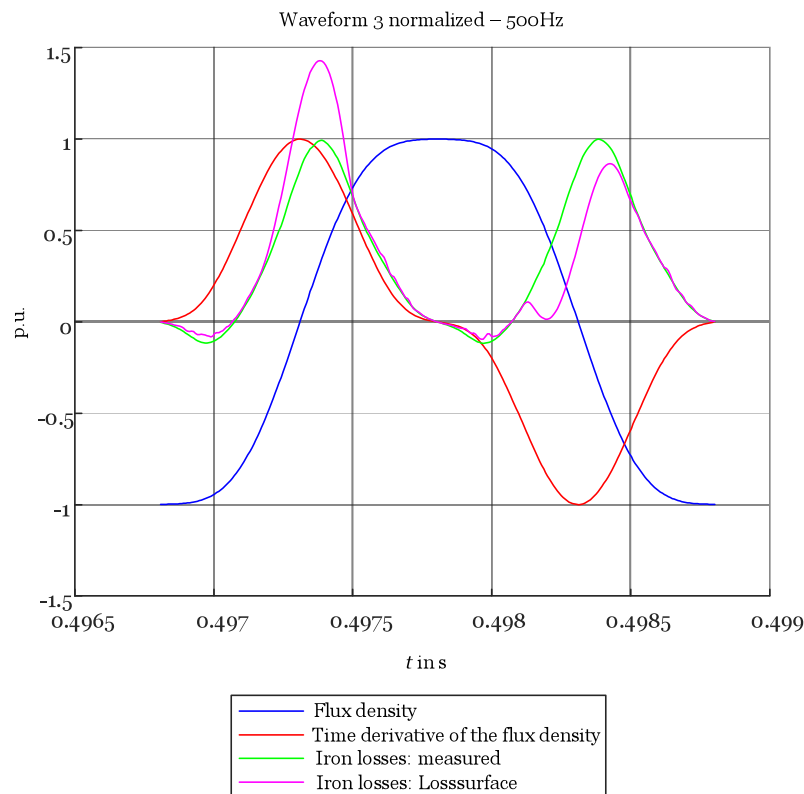


Figure 4.6: Normalized curve shapes of the third waveform at 500 Hz.

Normally when the loss surface approach is used to estimate the iron losses, no measurements are available to compare the results. So only signals with parameters, which are within the measured loss surface, should be used. As seen in Figure 4.6, waveforms which exceed the loss surface can lead to deviations. Figure 4.7 shows the supporting points of the loss surface in blue and the points of the third waveform with 500 Hz in red. Comparing Figure 4.6 and Figure 4.7 the biggest discrepancies occur for the parts, when the parameters of the flux density are in regions where

there are no supporting points of the loss surface. So if B or $\frac{dB}{dt}$ of the flux density waveform exceed the loss surface, a warning is issued and the user can decide whether he trusts the result, when the parameters of the flux density waveform only exceed the loss surface a little bit, or discard it when the parameters exceed the loss surface too much, such as in Figure 4.7.

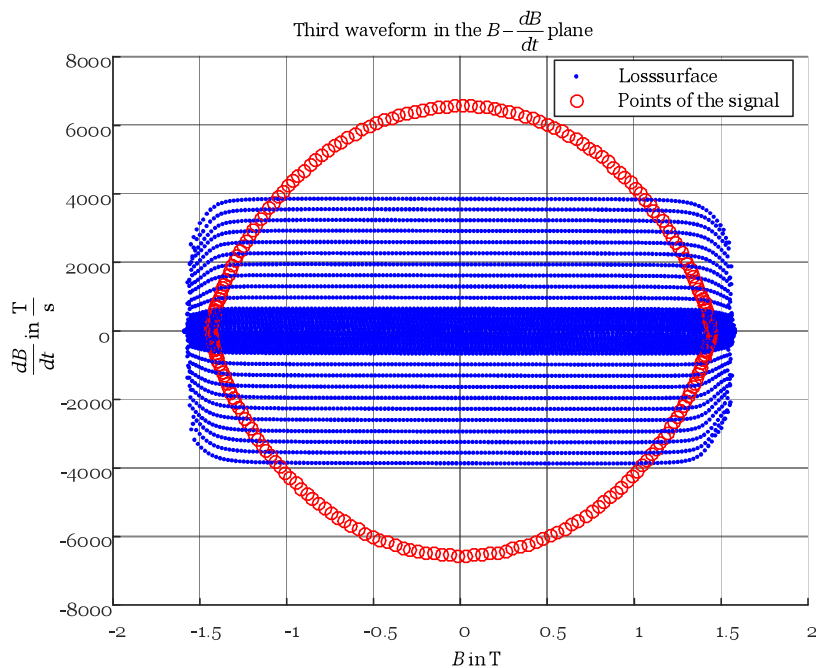


Figure 4.7: Points of the loss surface and the third signal at 500 Hz in the B - $\frac{dB}{dt}$ plane.

When the parameters of the desired flux density waveform are within the loss surface, the loss surface approach shows a good accordance with the measurement results. The error for waveforms with parameters which exceed the loss surface could also be very small, but for the reasons mentioned before, the user should decide from case to case if the results are reliable.

4.4 Conclusion

The aim of this thesis was to find and implement iron loss calculation methods. After a widespread literature research the improved generalized Steinmetz equation (iGSE) and the loss surface approach were chosen. As the comparison of the two iron loss calculation methods shows, both work well and give a good approximation of the iron losses for a known flux density distribution. The iGSE does not need any measurements, when a data sheet is available and the Steinmetz parameters can be determined as shown in Section 2.5, but it only gives the absolute value of the iron losses. Whereas the loss surface approach delivers also the waveform of the iron losses over time, if it is from interest. As can be seen in Figure 4.7 supporting points for the loss surface at higher values of $\frac{dB}{dt}$ would be preferable. With the used power amplifier and the Epstein frame with a high number of windings, it was not possible to achieve the desired parameters of the flux density waveform, because the available power amplifier does not deliver the higher voltages as required. When ring shaped specimens are used, the number of windings can be chosen in a way that the desired parameters can be achieved, see (3.14) and (3.15). So it should be possible to support the loss surface in a wider range with measurement points.

Chapter 5

Outlook and further steps

5.1 Iterative learning control - ILC

The measurements to obtain the data for the loss surface were taken with a rectangular voltage shape, so a triangular flux density was the consequence. All measurements were taken without any control or correction of the voltage, respectively the flux density, because the design and implementation of a controller would be beyond the scope of this thesis. So especially for low frequencies, the shape of the resulting flux density differed from the desired one. The waveforms for a frequency of 10 Hz are shown in Figure 5.1.

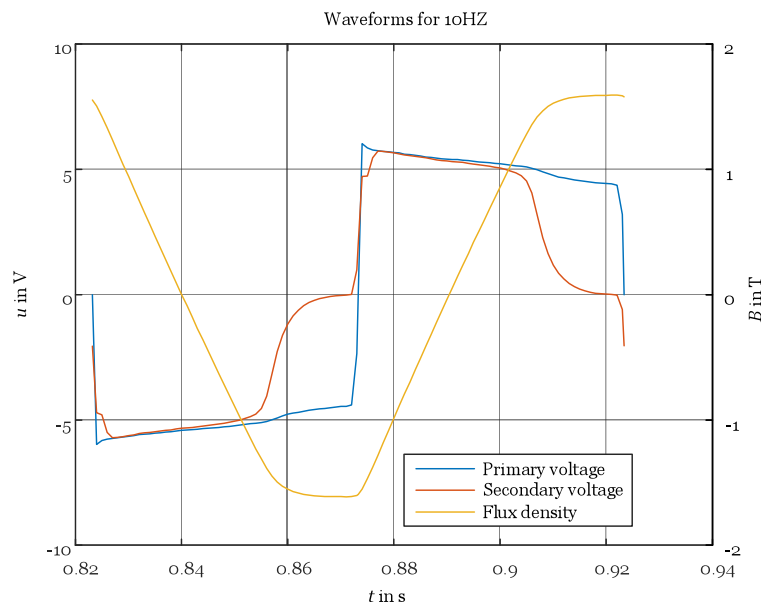


Figure 5.1: Voltage and flux density waveforms.

The shape of the flux density differs from the desired one. To obtain the desired shape of the flux density the primary voltage must be changed in an appropriate way, so a controller should be implemented. Because of the nonlinearity and the hysteresis behaviour of the iron, a linear controller would not work, so an other controller strategy must be used. Time is not a critical factor in this case, so also a slow controller could be used, as long as no quantity reaches a value which causes damage to a device of the used measurement setup. Additionally there are no constraints which would make a repetitive operation of the Epstein frame impossible. So iterative learning control (ILC) seems to be suitable for this task. The simplified control strategy is described in the following steps:

1. Estimate the initial waveform of the manipulated variable.
2. Apply the waveform on the controlled system.
3. Record the waveform of the control variable.
4. Calculate the the new waveform of the manipulated variable.
5. Repeat steps 2 to 4 until the error of the control variable is within an acceptable range.

A simple control law for the fourth step is given with

$$u_{i+1} = u_i + K \cdot e_i. \tag{5.1}$$

- u_{i+1} ... input of the system for the next iteration
- i ... number of the iteration
- u_i ... actual input of the system
- K ... gain factor
- e_i ... error during the i^{th} iteration

5.1.1 Desired distribution of the flux density

In Section 3.3 it was shown why triangular waveforms of the flux density are a appropriate choice to obtain the data for the loss surface. An ideal triangular waveform has a jump in its derivative and so would lead to an ideal square voltage in the secondary winding of the Epstein frame. With the limited bandwidth of the measurement setup such a waveform would not be manageable and the discontinuity could lead to problems for the control algorithm. So a waveform of the flux density which has a constant $\frac{dB}{dt}$ section by section and also no jump in its derivative would be preferable. These considerations lead to a triangular waveform which merges to a parabola on their tops, such as in the Figure 5.2.

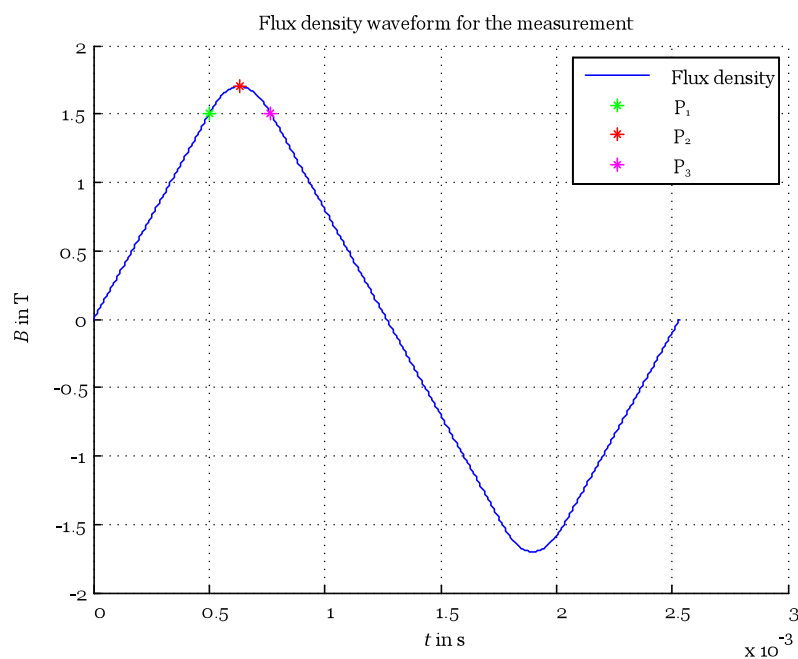


Figure 5.2: Waveform for the desired flux density.

The induced voltage in the secondary winding is the time derivative of the flux density, as can be seen in the Figure 5.3, there is no jump in the voltage so the rectangular transforms to a trapezoidal waveform.

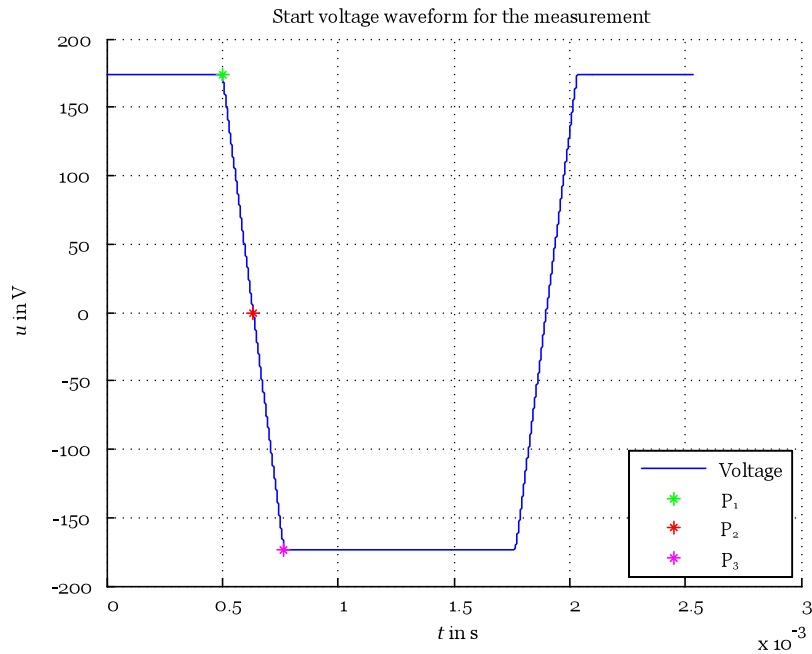


Figure 5.3: Start voltage waveform.

To create these waveform a MATLAB script was written, this script needs three parameters. The desired value of $\frac{dB}{dt}$, the maximum value of the flux density B_{\max} (at P_2 in Figure 5.2) and the value of the flux density, where straight merges in the parabola, B_1 (at P_1). The flux density in the linear region is given via

$$B(t) = k \cdot t + d. \quad (5.2)$$

Its time derivative is

$$\frac{dB}{dt} = k. \quad (5.3)$$

Since the time derivative is known, the first parameter k is known. Due to the fact that $B(t = 0) = 0$ d is also 0, so t_1 can be determined with

$$t_1 = \frac{B_1}{k}. \quad (5.4)$$

The parabola can be described with

$$B(t) = a \cdot t^2 + b \cdot t + c. \quad (5.5)$$

Again its time derivative

$$\frac{dB}{dt} = 2a \cdot t + b. \quad (5.6)$$

In P_1 the B and $\frac{dB}{dt}$ values of the straight and the parabola need to be the same, so 5.7 is valid

$$\begin{aligned} k &= 2at_1 + b \\ B_1 &= at_1^2 + bt_1 + c. \end{aligned} \quad (5.7)$$

At P_2 the flux density waveform has its maximum, so $\frac{dB}{dt} = 0$ and $B(t_2) = B_{\max}$ are valid

$$\begin{aligned} 0 &= 2at_2 + b \\ B_{\max} &= at_2^2 + bt_2 + c. \end{aligned} \quad (5.8)$$

With these relations the parameters t_2 , c , a and b can be determined

$$t_2 = \frac{1}{k} (2B_{\max} - B_1) \quad (5.9)$$

$$c = B_{\max} + \frac{kt_2^2}{2(t_1 - t_2)} \quad (5.10)$$

$$a = \frac{k}{2(t_1 - t_2)} \quad (5.11)$$

$$b = -2at_2. \quad (5.12)$$

Due to symmetry reasons

$$t_3 = 2t_2 - t_1. \quad (5.13)$$

From point P_3 until the flux density distribution reaches 0 again, $B(t)$ can be described with

$$B(t) = -kt + t_3k + B_1. \quad (5.14)$$

Because of the odd symmetry the second half wave is given with

$$B(-t) = -B(t). \quad (5.15)$$

With this flux density waveform and the assumption of linear material behaviour, the start voltage for the ILC can be calculated with

$$u_1 = NA \frac{dB}{dt}. \quad (5.16)$$

A waveform like this can be seen in Figure 5.3.

5.2 Ring shaped specimen

The measurements for the loss surface approach were carried out with a measurement setup based on an Epstein frame. As shown in Section 3.8.1 some disadvantages of the Epstein frame result from its construction and the assumptions which are made. To overcome these drawbacks measurements with ring shaped specimen of the material of interest should be made. This specimen form has several advantages compared to the Epstein frame:

- The whole specimen is magnetic active mass. The magnetic active mass for the Epstein frame has to be determined with $m_a = \frac{l_m}{4l}m$, where l_m is the agreed magnetic path length of 0.94 m, l is the length of the single strips of the specimen and m the whole mass of all specimens [31].
- The cross section is constant over the circumference [34]
- There are no sharp edges for the flux [34]
- In [14] it is stated that the ratio of the inner diameter to the outer diameter of the specimen should not remain under 0.8, l_{fe} can be assumed with a very small error as shown in (5.17) and so no correction of the path length as in Section 3.8.1 is necessary.

- The different cutting techniques have influence on the material properties [35]. If the size of the specimen match the dimensions of the single parts of the magnetic circuit of the considered drive and they are processed as the iron used in the drives, also the influence of the used cutting process can be considered.

The Epstein frame has a fixed number of windings, not so the ring specimen, so the number of windings has to be chosen in a way that they are appropriate for the used power source and measurement device. With an increasing number of primary windings the current decreases for a fixed magnetic field strength, but due to the fact that more windings are linked with the flux, the voltage, which has to be applied, is increasing. The induced voltage on the secondary side is influenced by the number of secondary windings, so the voltage range of the measurement device and the waveform of the flux density are the most important factors for the choice of the number of secondary windings. There is no compensation winding for the air flux, so the induced voltage in the secondary winding is linked with the flux density and not with the polarisation, such as it is the case with the Epstein frame. The mean length of the field lines can be calculated with [14]

$$l_{fe} = \frac{d_o + d_i}{2} \pi. \quad (5.17)$$

The magnetic field strength for a measured current can be calculated with (3.7). As mentioned before there is no compensation winding and the flux density can be calculated with the voltage in the secondary winding with

$$B = \frac{1}{N_2 A_{fe}} \int u_2 dt + B_0. \quad (5.18)$$

When the specimen is demagnetized before the measurement B_0 is 0. The evaluation of the measurement data for the loss surface is pretty much the same as with the measurement with the Epstein frame. The only difference is that the ring shaped specimen has no compensation winding and so also the air flux contributes to the induced voltage in the secondary winding, see (3.8) and (5.18).

5.2.1 FEM simulations for the ring shaped specimen

The simple geometry of the ring shaped specimen is easy to model in a FEM program. For some FEM programs it is not possible to choose the method or the used data,

which describe the iron, for the iron loss calculation, so the measurements on the ring shaped specimen can be used in different ways.

- The FEM program can be used to calculate the iron losses in the ring shaped specimen and so another tool for the verification of the two implemented iron loss calculation methods is given.
- It is possible to verify the ability of the iron loss calculation tool of the FEM program with the measurements on the ring shaped specimen, whether it can handle complex waveforms.

5.3 Conclusion

The aim of this thesis was to find and implement iron loss calculation methods for fractional horsepower motors. For this task the iGSE and the loss surface approach were chosen, in Chapter 4 it is shown that both work well. With a bit additional work, as shown in Chapter 5, the tool for the iron loss calculation could be integrated in the existing models of the fractional horsepower electric motors. The new iron loss models should make the motor models more accurate without the protracted need for FEM simulations.

Bibliography

- [1] J. R. H. Jr. and T. Miller, *Design OF BRUSHLESS PERMANENT-MAGNET MOTORS*. Magna Physics Publications and Oxford Science Publication, 1994.
- [2] C. P. Steinmetz, "On the law of hysteresis (part ii.) and other phenomena of the magnetic circuit," *Transactions of the American Institute of Electrical Engineers*, vol. IX, no. 1, pp. 619–758, Jan. 1892.
- [3] A. Brockmeyer and L. Schulting, "Modelling of dynamic losses in magnetic material," in *5th European Conference on Power Electronics and Applications*, Brighton, UK., Sep. 1993, pp. 112–117.
- [4] M. Albach, T. Durbaum, and A. Brockmeyer, "Calculating core losses in transformers for arbitrary magnetizing currents a comparison of different approaches," in *Power Electronics Specialists Conference*, Baveno, It., Jun. 1996, pp. 1463–1468.
- [5] J. Reinert, A. Brockmeyer, and R. W. A. A. D. Doncker, "Calculation of losses in ferro- and ferrimagnetic materials based on the modified Steinmetz equation," *IEEE Transactions on Industry Applications*, vol. 37, no. 4, pp. 1055–1061, Jul./Aug. 2001.
- [6] K. Venkatachalam, C. R. Sullivan, T. Abdallah, and H. Tacca, "Accurate prediction of ferrite core loss with nonsinusoidal waveforms using only Steinmetz parameters," in *IEEE Workshop on Computers in Power Electronics*, Mayaguez, Puerto Rico, US., Jun. 2002, pp. 36–41.
- [7] M. Mu and F. C. Lee, "A new core loss model for rectangular ac voltages," in *Energy Conversion Congress and Exposition (ECCE)*, Pittsburgh, Pennsylvania , US., Sep. 2014, pp. 5214–5220.
- [8] A. V. den Bossche and V. C. Valchev, *Inductors And Transformers For Power Electronics*. Taylor & Francis Group, 2005.

- [9] A. Krings, "Iron losses in electrical machines - influence of material properties, manufacturing processes, and inverter operation," Ph.D. dissertation, KTH School of Electrical Engineering, 2014.
- [10] J. Muhlethaler, J. Biela, J. W. Kolar, and A. Ecklebe, "Improved core-loss calculation for magnetic components employed in power electronic systems," *IEEE Transactions on Power Electronics*, vol. 27, no. 2, pp. 964–973, Jul. 2011.
- [11] E. C. Snelling, *Soft Ferrites, Properties and Applications*. Iliffe Books Ltd, 1969.
- [12] J. B. Goodenough, "Summary of losses in magnetic materials," *IEEE Transactions on Magnetics*, vol. 38, no. 5, pp. 3398–3408, Dec. 2002.
- [13] D. Andessner, R. Kobler, J. Passenbrunner, and W. Amrhein, "Measurement of the magnetic characteristics of soft magnetic materials with the use of an iterative learning control algorithm," in *Vehicle Power and Propulsion Conference*, Chicago, Illinois, US., Sep. 2011.
- [14] G. Bramerdorfer and D. Andessner, "Accurate and easy to obtain iron loss model for electric machine design," *IEEE Transactions on Industrial Electronics*, vol. 64, no. 3, pp. 2530–2537, Jun. 2016.
- [15] L. Li, A. Kedous-Lebouc, A. Foggia, and J. C. Mipo, "An iron loss model (loss surface) for feco sheet and its application in machine design," in *19th International Conference on Electrical Machines (ICEM)*, Rome, It., Sep. 2010.
- [16] T. Chevalier, A. Kedous-Lebouc, B. Cornut, and C. Cester, "A new dynamic hysteresis model for electrical steel sheet," *Physica B: Condensed Matter*, vol. 275, no. 1-3, pp. 197–201, Jan. 2000.
- [17] H. Jordan, "Die ferromagnetischen Konstanten für schwache Wechselfelder," *Elektrische Nachrichtentechnik*, vol. 1, p. 8, 1924.
- [18] M. C. Levin, "Charakterisierung von weichmagnetischen Pulververbundwerkstoffen für den Einsatz in Traktionsantrieben," Ph.D. dissertation, Technische Universität München, 2014.
- [19] G. Bertotti, "General properties of power losses in soft ferromagnetic materials," *IEEE Transactions on Magnetics*, vol. 24, no. 1, pp. 621–630, Jan. 1988.

-
- [20] J. P. A. Bastos and N. Sadowski, *Magnetic Materials and 3D Finite Element Modeling*. CRC Press, 2013.
- [21] I. D. Mayergoyz, *Mathematical Models of Hysteresis and Their Applications*. Elsevier, 2003.
- [22] M. Ruderman and T. Bertram, "Identification of soft magnetic B-H characteristics using discrete dynamic Preisach model and single measured hysteresis loop," *IEEE Transactions on Magnetics*, vol. 48, no. 4, pp. 1281–1284, Apr. 2012.
- [23] D. C. Jiles and J. B. Thoelke, "Theory of ferromagnetic hysteresis: determination of model parameters from experimental hysteresis loops," *IEEE Transactions on Magnetics*, vol. 25, no. 5, pp. 3928–3930, Sep. 1989.
- [24] F. R. Fulginei, G. M. Lozito, S. Gaiotto, and A. Salvini, "Improving the Jiles-Atherton model by introducing a full dynamic dependence of parameters," in *1st International Forum on Research and Technologies for Society and Industry Leveraging a better tomorrow (RTSI)*, Turin, It., Sep. 2015, pp. 161–165.
- [25] G. Torrisi, S. Mariéthoz, and R. Smith, "Identification of magnetic characteristics of induction motors based on the jiles-atherton model," in *16th European Conference on Power Electronics and Applications*, Lappeenranta, Fi., Aug. 2014.
- [26] J. Muhlethaler, J. Biela, J. Walter, and A. Ecklebe, "Core losses under the dc bias condition based on Steinmetz parameters," *IEEE Transactions on Power Electronics*, vol. 27, no. 2, pp. 953–963, Feb. 2011.
- [27] voestalpine, "isovac 250-35A datasheet," Oct. 2015.
- [28] X. Jannot, J. C. Vannier, A. Kedous-Lebouc, C. Marchand, M. Gabsi, and J. Saint-Michel, "Analytical computation of stator iron losses in interior permanent-magnet synchronous machine," in *19th International Conference on Electrical Machines (ICEM)*, Rome, It., Sep. 2010.
- [29] G. Ugalde, G. Almandoz, J. Poza, and A. Gonzalez, "Computation of iron losses in permanent magnet machines by multi-domain simulations," in *13th European Conference on Power Electronics and Applications*, Barcelona, Es., Sep. 2009.

- [30] T. Chevalier, A. Kedous-Labouc, B. Cornut, and C. Cester, "Estimation of magnetic loss in an induction motor fed with sinusoidal supply using a finite element software and a new approach to dynamic hysteresis," *IEEE Transactions on Magnetics*, vol. 35, no. 5, pp. 3400–3402, Sep. 1999.
- [31] *Magnetische Werkstoffe Teil 2: Verfahren zur Bestimmung der magnetische Eigenschaften von Elektroblech und -band mit Hilfe eines Epsteinrahmens*, OVE Std. IEC 60 404-2:1996 + A1:2008, Rev. 2009-02-01, Feb. 2009.
- [32] Z. Xu, J. Guan, and J. Zhou, "A distributed inverse distance weighted interpolation algorithm based on the cloud computing platform of hadoop and its implementation," in *12th International Conference on Fuzzy Systems and Knowledge Discovery (FSKD)*, Zhangjiajie, Cn., Aug. 2015, pp. 2412–2416.
- [33] M. J. D. Powell, "Some algorithm for thin plate spline interpolation to functions of two variables," in *Conference on Advances in Computational Mathematics*, New Delhi, In., Jan. 1993.
- [34] J. Sievert, "The magnetic properties of electrical sheet steel - physical, statistical and standards aspects of measurements," in *Coil Winding Insulation and Electrical Manufacturing Exhibition*, Berlin, De., May 2016.
- [35] M. Bali, "Magnetic material degradation due to different cutting techniques and its modeling for electric machine design," Ph.D. dissertation, Technische Universität Graz, 2016.
- [36] Z. Godec, "Effect of various stress-relief annealing treatments on permeability and aging of grain-oriented electrical steel strips," *IEEE Transactions on Magnetics*, vol. 14, no. 1, pp. 4–8, Jan. 1978.
- [37] H. Ahlers and J. Sievert, "Comparison of a single strip tester and Epstein frame measurements," *Journal of Magnetism and Magnetic Materials*, vol. 26, no. 1-3, pp. 176–178, Mar. 1982.
- [38] voestalpine, "isovac 270-35A datasheet," Feb. 2015.

List of figures

1.1	Trapezoidal flux density and its time derivative.	6
1.2	Single losses as a function of the frequency [20].	10
1.3	Hysterion with the switching thresholds α and β	11
1.4	Parallel connection of single hysterons [21].	12
2.1	First level subloop.	18
2.2	Second level subloop.	19
2.3	Nested loops in the hysteresis loop.	20
2.4	Mainloop of the testsignal.	22
2.5	Subloop of the signal.	23
2.6	Sinusoidal signal with a frequency of 500 Hz and an amplitude of 1100 mT.	25
2.7	Trapezoidal approximation for the flux density in the yoke.	28
2.8	Comparison with one set of Steinmetz parameters.	32
2.9	Comparison with three sets of Steinmetz parameters.	33
2.10	Comparison at 700 Hz.	35
3.1	Loss surface for isovac 800-35A.	38
3.2	Supporting points for one sinusoidal flux density with $B = 1$ T and $f = 10$ Hz.	39
3.3	Supporting points for sinusoidal flux densities.	40
3.4	Supporting points for triangular flux densities.	41
3.5	Triangular flux density waveform.	41
3.6	Primary voltage and flux density for 300 Hz.	42
3.7	Block diagram of the measurement setup.	43
3.8	Used measurement setup.	44
3.9	Primary and secondary voltage for 50 Hz with sense line on the secondary side.	46
3.10	Primary current for 50 Hz with sense line on the secondary side.	47

3.11	Primary and secondary voltage for 500 Hz with sense line on the secondary side.	47
3.12	Primary current for 500 Hz with sense line on the secondary side. . .	48
3.13	Primary and secondary voltage for 50 Hz with sense line on the output of the power amplifier.	48
3.14	Primary current for 50 Hz with sense line on the output of the power amplifier.	49
3.15	Primary and secondary voltage for 500 Hz with sense line on the output of the power amplifier.	49
3.16	Primary current for 500 Hz with sense line on the output of the power amplifier.	50
3.17	Equivalent circuit of the Epstein frame.	52
3.18	Simplified equivalent circuit of the Epstein frame.	52
3.19	Surface for the IDWI with $n = 4$ and $p = 0.1$	57
3.20	TPSI surface for isovac 270-35A.	60
3.21	Basic structure of an Epstein frame [20].	61
3.22	Magnetic path length of the Epstein frame.	62
4.1	Decomposition of waveform 2 of Table 4.1.	66
4.2	First waveform of Table 4.1.	67
4.3	Second waveform of Table 4.1.	67
4.4	Third waveform of Table 4.1.	68
4.5	Normalized curve shapes of the third waveform.	70
4.6	Normalized curve shapes of the third waveform at 500 Hz.	71
4.7	Points of the loss surface and the third signal at 500 Hz in the B - $\frac{dB}{dt}$ plane.	72
5.1	Voltage and flux density waveforms.	75
5.2	Waveform for the desired flux density.	77
5.3	Start voltage waveform.	78

List of tables

1.1	Extended version of the table in [9].	15
2.1	Parameters for N87 [26].	21
2.2	Comparison of the results for the first testsignal.	24
2.3	Parameters for isovac 250-35 A at 500 Hz.	25
2.4	Comparison of the results for the second testsignal in $\frac{kW}{m^3}$	26
2.5	Comparison of the results for the second testsignal in $\frac{W}{kg}$ with the data sheet [27].	27
2.6	Parameters for isovac 250-35 A at 60 Hz	29
2.7	Comparison of the results for testsignal 3.	30
2.8	Excerpt of the table for 60 Hz from the data sheet [27].	31
2.9	One set of Steinmetz parameters per frequency.	32
2.10	Three sets of Steinmetz parameters per frequency.	34
3.1	Used measurement devices.	45
4.1	Primary voltage forms.	66
4.2	Comparison of the results.	69